Abrupt excursions in water vapor isotopic variability at the Pointe Benedicte observatory on Amsterdam Island

Amaëlle Landais[1,*], Cécile Agosta[1,*], Françoise Vimeux[1,2], Olivier Magand[3], Cyrielle Solis[1], Alexandre Cauquoin[4], Niels Dutrievoz[1], Camille Risi[5], Christophe Leroy-Dos Santos[1], Elise Fourré[1], Olivier Cattani[1], Olivier Jossoud[1], Bénédicte Minster[1], Frédéric Prié[1], Mathieu Casado[1], Aurélien Dommergue[6], Yann Bertrand[6], Martin Werner[7]

[1] Laboratoire des Sciences du Climat et de l'Environnement, LSCE/IPSL, CEA-CNRS-UVSQ, Université Paris-Saclay, 91191 Gif-sur-Yvette, France

[2] HydroSciences Montpellier (HSM), UMR 5569 (UM, CNRS, IRD), 34095 Montpellier, France

[3] Observatoire des Sciences de l'Univers à La Réunion (OSU-R), UAR 3365, CNRS, Université de La Réunion, Météo France, IRD, 97744 Saint-Denis, La Réunion, France

[4] Institute of Industrial Science (IIS), The University of Tokyo, Kashiwa, Japan.

[5] Laboratoire de Météorologie Dynamique, Institut Pierre - Simon Laplace, Sorbonne Université / CNRS / École Polytechnique – IPP, Paris, France

[6] Univ. Grenoble Alpes, CNRS, INRAE, IRD, Grenoble INP$^{\intercal}$, IGE, 38000 Grenoble, France ($^{\intercal}$Institute of Engineering and Management Univ. Grenoble Alpes)

[7] Alfred Wegener Institute, Helmholtz Centre for Marine and Polar Research, D-27570 Bremerhaven, Germany

* corresponding authors who contributed equally to the study: amaelle.landais@lsce.ipsl.fr and cecile.agosta@lsce.ipsl.fr

Abstract

In order to complement the picture of the atmospheric water cycle in the Southern Ocean, we have continuously monitored water vapor isotopes since January 2020 on Amsterdam Island in the Indian Ocean. We present here the first 2-year-long water vapor isotopic record on this site. We show that the water vapor isotopic composition largely follows the water vapor mixing ratio, as expected in marine boundary layers. However, we detect 11 periods of a few days where there is a strong loss of correlation between water vapor $\delta^{18}O$ and water vapor mixing ratio as well as abrupt negative excursions of water vapor $\delta^{18}O$. These excursions often occur toward the end of precipitation events. Six of these events show a decrease in gaseous elemental mercury suggesting subsidence of air from higher altitude.

Our study aims at further exploring the mechanism driving these negative excursions in water vapor $\delta^{18}O$. We used two different models to provide a data-model comparison over this 2-year period. While the European Centre Hamburg model (ECHAM6-wiso) at 0.9° was able to reproduce most of the sharp negative water vapor $\delta^{18}O$ excursions hence validating the physics process and isotopic implementation in this model, the Laboratoire de Météorologie Dynamique Zoom model (LMDZ-iso) at 2° (3°) resolution was only able to reproduce 7 (1) of the negative excursions highlighting the possible influence of the model resolution for the study of such abrupt isotopic events. Based on our detailed model-data comparison, we conclude that the most plausible explanations for such isotopic excursions are rain-vapor interactions associated with subsidence at the rear of a precipitation event.

1. Introduction

The main sources of uncertainty in the atmospheric components of Earth System Models for future climate projections are associated with complex atmospheric processes, particularly those related to water vapor and clouds (Arias et al., 2021; Sherwood et al., 2014). Decreasing these uncertainties is of vital interest as the hydrological cycle is a fundamental element of the climate system because it allows, via the transport of water vapor, to ensure the Earth's thermal balance.

Stable water isotopes are a useful tool to study the influence of dynamical processes on the water budget at various spatial and temporal scales. They provide a framework for analyzing moist processes over a range of time scales from large-scale moisture transport to cloud formation, precipitation, and small-scale turbulent mixing (Bailey et al., 2023; Dahinden et al., 2021; Galewsky et al., 2016; Thurnherr et al., 2020).

The relative abundance of heavy and light isotopes in different water reservoirs is altered during phase change processes due to isotopic fractionation (caused by a difference in saturation vapor pressure and molecular diffusivity in the air and the ice). Each time a phase change occurs, the relative abundance of water vapor isotopes is altered. We express the abundance of the heavy isotopes D and ^{18}O with respect to the amount of light isotopes H and ^{16}O, respectively, in the water molecules through the notation δ:

$$\delta^{18}O = \left(\frac{\left({}^{18}O/{}^{16}O \right)_{Sample}}{\left({}^{18}O/{}^{16}O \right)_{VSMOW}} - 1 \right) \times 1000 \qquad \text{(Eq. 1)}$$

$$\delta D = \left(\frac{\left(D/H \right)_{Sample}}{\left(D/H \right)_{VSMOW}} - 1 \right) \times 1000 \qquad \text{(Eq. 2)}$$

where (^{18}O/^{16}O) and (D/H) represent the isotopic ratios of oxygen and hydrogen atoms in water and VSMOW (Vienna Standard Mean Ocean Water) is an international reference standard for water isotopes.

There are two types of isotopic fractionation: equilibrium fractionation, which is caused by the difference in saturation vapor pressure of different isotopes, and non-equilibrium fractionation, which occurs due to molecular diffusion (e.g. during ocean evaporation in undersaturated atmosphere or snowflakes condensation in oversaturated atmosphere). In the water vapor above the ocean, the proportion of non-equilibrium fractionation, and hence diffusive processes can

be estimated by the deuterium excess, a second order isotopic variable denoted d-excess, defined as (Dansgaard, 1964):

$$\text{d-excess} = \delta D - 8 \times \delta^{18}O \qquad \text{(Eq.3)}$$

Over the recent years and thanks to the development of optical spectroscopy enabling continuous measurements of water isotopes ratios in water vapor, an increasing number of studies have focused on the use of water vapor stable isotopes to document the dynamics of the water cycle over synoptic weather events, such as cyclones, cold fronts, atmospheric rivers (Aemisegger et al., 2015; Ansari et al., 2020; Bhattacharya et al., 2022; Dütsch et al., 2016; Graf et al., 2019; Lee et al., 2019; Munksgaard et al., 2015; Tremoy et al., 2014) or water cycle processes such as evaporation over the ocean or deep convection (Benetti et al., 2015; Bonne et al., 2019). Several instruments have been installed either in observatory stations (e.g. Aemisegger et al., 2012; Guilpart et al., 2017; Leroy-Dos Santos et al., 2020; Steen-Larsen et al., 2013; Tremoy et al., 2012), on boat (e.g. Benetti et al., 2014; Thurnherr et al., 2019) or on aircraft (Henze et al., 2022). In the aforementioned studies, the interpretation of the isotopic records is often performed using a hierarchy of isotopic models, from conceptual models (Rayleigh type) to general circulation models or regional weather prediction models equipped with water isotopes (Ciais and Jouzel, 1994; Markle and Steig, 2022; Risi et al., 2010; Werner et al., 2011). Such data comparisons enable one to test the performances of the models either in the simulation of the dynamic of the atmospheric water cycle or in the implementation of the water isotopes. Our study is part of these dynamics analyses and aims at improving the documentation of climate and atmospheric water cycle in the Southern Indian Ocean, a region which has been poorly documented until now.

Over the previous years, we have installed three water vapor analyzers on La Reunion Island at the Maïdo observatory, 21.079°S, 55.383°E, 2160m (Guilpart et al., 2017) and in Antarctica (Dumont d'Urville, 66,663°S, 140°E, 202m and Concordia, 75.1°S, 123.333°E, 3233m; Bréant et al., 2019; Casado et al., 2016; Leroy-Dos Santos et al., 2021). These instruments have been used for the following purposes. They document the diurnal variability of the isotopic signal with the influence of the subtropical westerly jet on the water isotopic signal in night as well as the cyclonic activity on La Réunion Island. In Antarctica, the records have shown a strong influence of katabatic winds on the isotopic composition of water vapor (Bréant et al., 2019). In order to complete the picture of the atmospheric water cycle over the Indian basin of the Southern Ocean already measured by these three analyzers, we installed a new water vapor

isotopic analyzer ~~in the~~at mid-latitude ~~of~~in the south Indian Ocean on Amsterdam Island (Figure 1) in November 2019. Amsterdam Island is one of the very rare atmospheric observatories in the southern hemisphere. Moreover, the south Indian Ocean is a significant moisture source for Antarctic precipitation, notably in the region encompassing Dumont d'Urville and Concordia stations (Jullien et al., 2020; Wang et al., 2020).

The objective of this study is to provide the first analyses of isotopic records (vapor and precipitation) on Amsterdam Island, with a comparison of meteorological data and environmental data collected in parallel on the Amsterdam Island Observatory (e.g. atmospheric mercury) to help with the interpretation of isotopic records. Indeed, previous studies have shown that gaseous elemental mercury decreases with increasing altitude in marine environment suggesting that gaseous elemental mercury can be used as a tracer of subsidence of air from the high altitude (e.g. Koening et al., 2023). This study includes analyses of meteorological maps, back trajectories as well as outputs from general circulation models equipped with water isotopes. After a description of the different records over the years 2020 and 2021, model simulations and back trajectories, we focus on some low-pressure events associated with a strong negative excursion of $\delta^{18}O_v$ over a few days and a decoupling between $\delta^{18}O_v$ and humidity. These events are then used for evaluation of ~~to evaluate~~ atmospheric component of Earth system models ~~-~~equipped with water isotopes.

2. Methods

2.1 Site

Labelled as a global site for the Global Atmosphere Watch World Meteorological Organization, Amsterdam Island (37.7983° S, 77.5378° E) is a remote and very small island of 55 km^2 with a population of about 30 residents, located in the southern Indian Ocean at 3300 km and 4200 km downwind from the nearest lands, Madagascar, and South Africa, respectively (Sprovieri et al., 2016). Climate is temperate, generally mild with frequent presence of clouds (average total sunshine hours is 1581 hours per year over the period 1981 – 2010 from MeteoFrance data). Seasonal boundaries are defined as follows: winter from July to September and summer from December to February, in line with previous studies (Sciare et al., 2009). Average temperature is lower in winter compared to summer (10.5°C vs 15°C) while relative humidity and wind speed remain high (50-85% and 5 to 15 m s^{-1} respectively) most of the year without a clear seasonal cycle.

Numerous atmospheric compounds and meteorological parameters are and were continuously monitored at the site since 1960 (Angot et al., 2014; El Yazidi et al., 2018; Gaudry et al., 1983; Gros et al., 1999, 1998; Polian et al., 1986; Sciare et al., 2000, 2009; Slemr et al., 2015; Slemr et al., 2020). In particular, the Amsterdam (AMS) site hosts several dedicated atmospheric observation instruments notably at the Pointe Bénédicte atmospheric observatory (70 m above sea level) where greenhouse gases concentrations and mercury (Hg) are monitored. Hg species have been continuously measured since 2012.

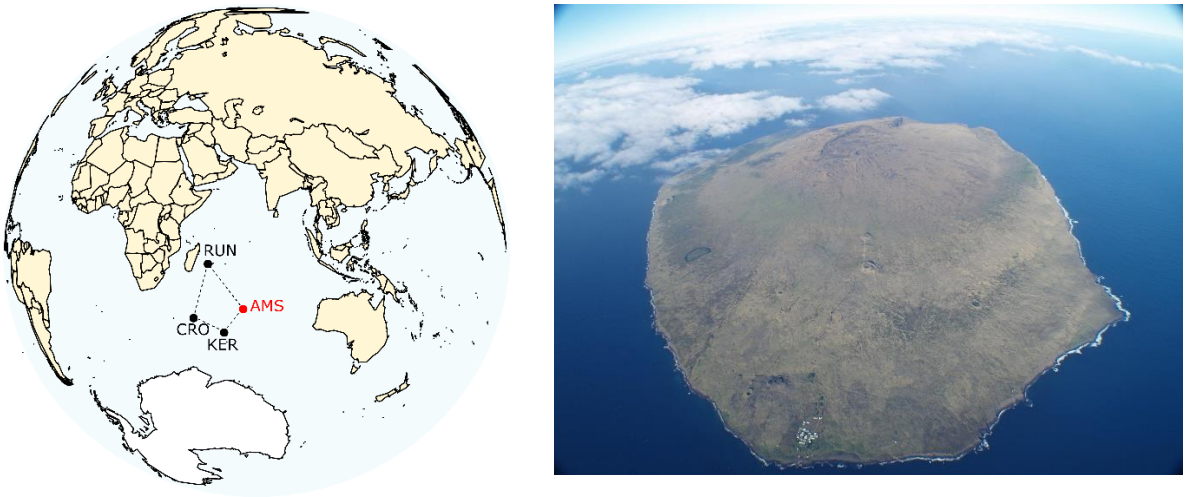

Figure 1 : Location (left) and picture (right) of Amsterdam Island. CRO: Crozet Island; RUN: La Réunion Island; KER: Kerguelen Island; AMS: Amsterdam Island.
Picture credit: left – from O. Magand adapted from (Angot et al., (2016); right – photo taken by O. Magand.

2.2 Long term measurements

2.2.1 Meteorological measurements

One meteorological station is installed at the top of an observation mast (25 m above ground level, hence 95 m above sea level) at the Pointe Bénédicte observatory since 1980 (data used during this study). Wind speed and direction, atmospheric pressure, air temperature and relative humidity data are currently obtained at a minute resolution. Another meteorological station is based on the island and is operated by Météo France at Martin-de-Viviès life base around 27 m

above sea level, about two kilometers east from the Pointe Bénédicte observatory collecting air temperature, humidity, precipitation, wind speed and direction, pressure and solar radiation

2.2.2 Gaseous elemental mercury (GEM)

Atmospheric GEM (Gaseous Elemental Mercury) measurements have been conducted since 2012 in the framework of IPEV GMOStral-1028 observatory program at the Pointe Benedicte atmospheric research facility (Magand and Dommergue, 2022). GEM is continuously measured (15-minute data frequency acquisition) using a Tekran 2537 A/B instrument model (Angot et al., 2014; Li et al., 2023; Slemr et al., 2015, 2020; Sprovieri et al., 2016). The measurement is based on mercury enrichment on a gold cartridge, followed by thermal desorption and detection by cold vapor atomic fluorescence spectroscopy (Bloom and Fitzgerald, 1988; Fitzgerald and Gill, 1979). Concentrations are expressed in nanograms per cubic meters at standard temperature and pressure conditions (273.15 K and 1013.25 hPa) with an instrumental detection limit below 0.1 ng m^{-3} and a GEM average uncertainty value around 10% (Slemr et al., 2015). The instrument is automatically calibrated following a strict procedure adapted from that of Dumarey et al. (1985). Ambient air is sampled at 1.2 L min^{-1} through a heated (50°C) and UV protected PTFE sampling line, with an inlet installed outside, 6 m above ground level (76 m above sea level). The air is filtered through two 0.45 µm pore size polyether sulphone and one PTFE (polytetrafluoroethylene) 47 mm diameter filters before entering in Tekran to prevent the introduction of any particulate material into the detection system as well as to capture any gaseous oxidized mercury or particulate bound mercury species ensuring that only GEM is sampled. To ensure the comparability of mercury measurements around the world, the instrument is operated according to the Global Mercury Observation System standard operating procedures (Sprovieri et al., 2016; Steffen et al., 2012).

In this study, and even ~~if~~ though long-range transport and a variable tropopause height may modulate the signal, atmospheric GEM is used as potential tracer of stratosphere-to-troposphere intrusion and/or subsidence of upper troposphere air (above 5-6 km) that may impact the atmospheric records at the Pointe Benedicte Observatory where marine boundary layer air is collected most of the time (Angot et al., 2014; Slmer et al., 2015, 2020; Sprovieri et al., 2016). Mercury in the atmosphere consists of three forms: gaseous elemental mercury (GEM as defined above), gaseous oxidized mercury and particulate-bound mercury. GEM, the dominant form of atmospheric mercury, is ubiquitous in the atmospheric reservoir and originates from a multitude of anthropogenic and natural sources (Edwards et al., 2021; Gaffney et al., 2014;

Gustin et al., 2020 ; Gworek et al., 2020). Near the surface (marine or terrestrial boundary layer) and out of polar regions, gaseous oxidized mercury and particulate-bound mercury represent only a few percent of the total atmospheric mercury (Gustin and Jaffe, 2010; Gustin et al., 2015; Swartzendruber et al., 2006). Chemical cycling and spatiotemporal distribution of mercury in the air is still poorly understood whatever atmospheric layer considered (surface, mixed or free troposphere, stratosphere), and complete GEM oxidation schemes remain unclear (Shah et al., 2021 and associated references). Still, several studies provided evidence that vertical distribution of atmospheric mercury measurements from boundary layer to lower/upper troposphere and stratosphere shows a decreasing trend in GEM concentration with increasing altitude, in parallel with an increase in the concentration of divalent mercury resulting from GEM oxidation mechanisms (Brooks et al., 2014; Fain et al., 2009; Fu et al., 2016; Koenig et al., 2023; Lyman and Jaffe, 2012; Murphy et al., 2006; Swartzendruber et al., 2006, 2008; Sheu et al., 2010; Talbot et al., 2007). The identification of such observational processes (lower concentration of GEM ~~concentrations~~ in high-altitude air masses compared to those in the ~~versus~~ marine boundary layer ones) is used here to help characteriz~~e~~ing possible intrusions of ~~high~~ high-altitude air masses ~~intrusions~~ at the low altitude Pointe Benedicte o~~O~~bservatory.

2.3 Water vapor isotopic measurements

The near-surface water vapor $\delta^{18}O$ and δD (hereafter $\delta^{18}O_v$ and δD_v expressed in ‰ versus SMOW and enabling to calculate water vapor d-excess$_v$ as d-excess$_v$ = $\delta D_v - 8\times\delta^{18}O_v$). ~~and t~~The water vapor mixing ratio (q_v in ppmv) have been measured continuously since November 2019. The measurements have been done with a Picarro Inc. instrument (L2130-i model) based on wavelength-scanned cavity ring down spectroscopy. The instrument has been installed in a temperature-controlled room at the Amsterdam Island observatory and the sampling of water vapor is done outside at ~ 6 m above ground level (or 76 m above sea level) through a 5 m long inlet tube made of PFA (perfluoroalkoxy alkanes) and heated at 40°C.

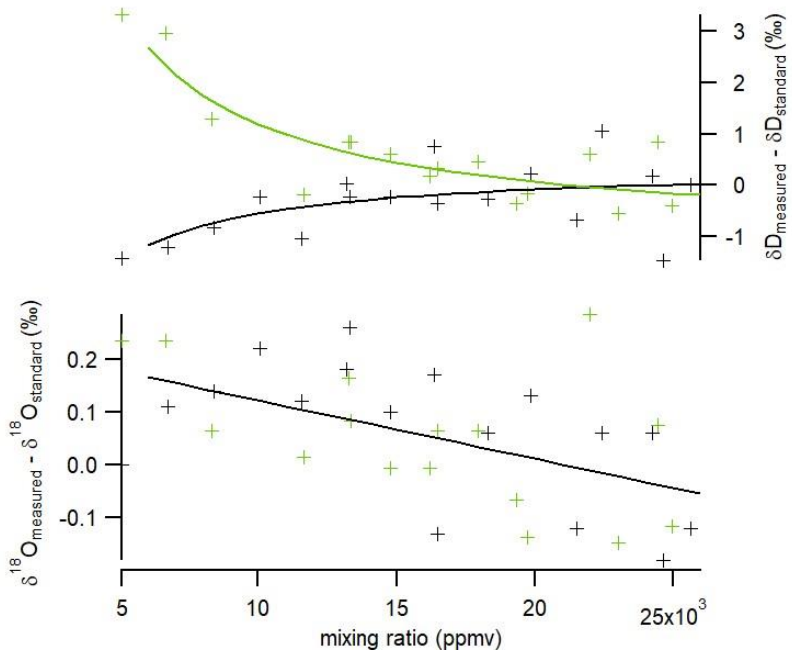

Figure 2: Influence of the water vapor mixing ratio on measured δD (top) and $\delta^{18}O$ (bottom) (anomaly from the true value of the standard). The results are shown for two different standards (GREEN_AMS in green and EPB_AMS in black). The crosses indicate the data obtained with the set-up and the solid lines are the best regression curves (same curve for $\delta^{18}O$ for both standards).

The calibration of water vapour mixing ratio was performed in the laboratory before sending the instrument to Amsterdam Island. In the field, we found an excellent agreement between mixing ratio measured by the Picarro instrument and mixing ratio measured by the weather station (the difference between the two records always stays below 2% and there is no systematic shift between the two records).

The calibration of the water isotopic data is performed in several steps following previous studies (Leroy-Dos Santos et al., 2020; Tremoy et al., 2011) and using a standard delivery module by Picarro. First, we quantified the influence of the water vapor mixing ratio on the water isotope ratios. This effect is large at very low humidity (Leroy-Dos Santos et al., 2021). It can also depend on the isotopic composition of the standard water (Weng et al., 2020). Here, we introduced two different water standards, EPB-AMS and GREEN-AMS, with respective values of (-5.66 ‰, -47.31 ‰) and (-32.65 ‰, -263.76 ‰) for the couple ($\delta^{18}O$, δD) which encompass the isotopic values observed on site. While we would expect a constant null value for ($\delta^{18}O_{measured}$- $\delta^{18}O_{standard}$) in Figure 2 because we always inject the same water standards, the measured $\delta^{18}O$ values of both EPB-AMS and GREEN-AMS standards in fact

decrease with increasing humidity with the same amplitude. The ($\delta D_{measured}$-$\delta D_{standard}$) displayed in Figure 2 also shows variations but in contrast to the relative evolution of $\delta^{18}O$ with respect to water vapor mixing ratio, the δD measurements of EPB-AMS and GREEN-AMS standards exhibit different behavior: δD of EPB-AMS increases by 1.5‰ and δD of GREEN-AMS decreases by 2.5 ‰ over the same 6,000-24,000 ppmv range for water vapor mixing ratio q_v.

As a consequence, the raw $\delta^{18}O_v$ measurements are corrected with the following regression:

$$\delta^{18}O_{v,corr} = \delta^{18}O_{v,measured} + 1.1.10^{-5} \times q + 0.232 \qquad \text{(Eq 4)}$$

For the correction of the raw δD_v, we use two different regression splines for EPB-AMS and GREEN-AMS (cf Figure 2):

$$\delta D_{EPB-AMS,corr} = \delta D_{EPB-AMS,measured} + \frac{9300}{q} - 0.383 \qquad \text{(Eq 5)}$$

$$\delta D_{GREEN-AMS,corr} = \delta D_{GREEN-AMS,measured} - \frac{22400}{q} + 1.05 \qquad \text{(Eq 6)}$$

The raw δD_v are thus weighted-corrected according to their distance to the EPB_AMS and the GREEN_AMS splines as follows:

$$\delta D_{v,corr} = \delta D_{GREEN-AMS,corr} + \frac{\delta D_{v,measured} - \delta D_{GREEN-AMS,measured}}{\delta D_{EPB-AMS,measured} - \delta D_{GREEN-AMS,measured}} \times (\delta D_{EPB-AMS,corr} - \delta D_{GREEN-AMS,corr}) \qquad \text{(Eq 7)}$$

This first calibration step (correction from the influence of mixing ratio on the isotopic composition) has been performed every year over the whole range of mixing ratio values and provided very similar results from one year to the other.The second calibration step consists in the injection of the same two isotopic standards every 47 h at a water vapor mixing ratio of 13,000 ppmv to correct for any long-term drift. The correction associated with this drift is less than 0.4 ‰ for $\delta^{18}O$ and 2.5 ‰ for δD over the two years of measurements.

Precipitation were also sampled on a weekly basis in a rain gauge filled with paraffin oil which permits to have measurements of water isotopic composition in the precipitation on a weekly basis. The water samples are then sent for analyses to LSCE (Laboratoire des Sciences du Climat et de l'Environnement) and measured with an isotopic analyzer L2130-i by Picarro. The uncertainty associated with this series of measurements is of ±0.15 ‰ for $\delta^{18}O$ and ±0.7 ‰ for δD leading to an uncertainty of ±1.4 ‰ for d-excess.

2.4 Back trajectories: FLEXPART

The origin and trajectory of air masses were calculated by FLEXPART, which is a Lagrangian particle dispersion model (Pisso et al., 2019). All the meteorological data used to simulate the back trajectories are taken from the ERA5 atmospheric reanalysis (Hersbach et al., 2020) with a 6-hourly resolution. The ERA5 reanalysis is carried out by the European Center for Medium-Range Weather Forecasts (ECMWF), using ECMWF's Earth System model IFS (Integrated Forecasting System), cycle 41r2. For a few selected events, we used FLEXPART to calculate back trajectories over 5 days with 1000 launches of neutral particles (sensitivity test) of inert air tracers released randomly (volume of 0.1°×0.1°×100 m) every 3 hours at 100 m above sea level (Leroy-Dos Santos et al., 2020) centered around the coordinates of Amsterdam Island. The results of the FLEXPART back trajectories are then displayed as particle probability density ~~probability~~ as well as through the location of their humidity weighted averages.

2.5 General atmospheric circulation model equipped with water stable isotopes

2.5.1 LMDZ-iso model (Laboratoire de Météorologie Dynamique Zoom model equipped with water isotopes)

LMDZ-iso (Risi et al., 2010) is the isotopic version of the atmospheric general circulation model LMDZ6 (Hourdin et al., 2020). We have used LMDZ-iso version 20230111.trunk with the physical package NPv6.1, identical to the atmospheric setup of IPSL-CM6A (Boucher et al., 2020) used for phase 6 of the Coupled Model Intercomparison Project (CMIP6, Eyring et al., 2016). We performed two simulations, one at very low horizontal resolution (VLR, 3.75° in longitude and 1.9° in latitude, 96×95 grid cells) and the second at low horizontal resolution (LR, 2.0° in longitude and 1.67° in latitude, 144×142 grid cells). Both simulations have 79

vertical levels and the first atmospheric level is located around 10 m above ground level. The LMDZ-iso 3D-fields of temperature and wind are nudged toward the 6-hourly ERA5 reanalysis data with a relaxation time of 3 hours. Surface ocean ~~surface~~ boundary conditions are taken from the monthly mean SST and sea-ice fields from the CMIP6 AMIP Sea Surface Temperature and Sea Ice dataset version 1.1.8 (Durack et al., 2022; Taylor et al., 2000). LMDZ-iso outputs are used at a 3-hourly resolution. Amsterdam Island (58 km^2) is too small to be represented in the LMDZ-iso model.

2.5.2 ECHAM6-wiso model (European Centre Hamburg model equipped with water isotopes)

ECHAM6-wiso (Cauquoin et al., 2019; Cauquoin and Werner, 2021) is the isotopic version of the atmospheric general circulation model ECHAM6 (Stevens et al., 2013). The implementation of the water isotopes in ECHAM6 has been described in detail by Cauquoin et al. (2019), and has been updated in several aspects by Cauquoin and Werner (2021) to make the model results more consistent with the last findings based on water isotope observations (isotopic composition of snow on sea ice considered, supersaturation equation slightly updated, and kinetic fractionation factors for oceanic evaporation assumed as independent of wind speed). We have used ECHAM6-wiso model outputs from a simulation with a T127L95 spatial resolution (0.9° horizontal resolution and 95 vertical levels). ECHAM6-wiso is thus run with a finer resolution than both LMDZ-iso simulations. The ECHAM6-wiso 3D-fields of temperature, vorticity and divergence as well as the surface pressure field were nudged toward the ERA5 reanalysis data ~~(Hersbach et al., 2020)~~ every 6 hours (Hersbach et al., 2020). The orbital parameters and greenhouse gas concentrations have been set to the values of the corresponding model year. The monthly mean sea surface temperature and sea-ice fields from the ERA5 reanalysis have been applied as ocean surface boundary conditions, as well as a mean $\delta^{18}O$ of surface seawater reconstruction from the global gridded data set of LeGrande and Schmidt (2006). As no equivalent data set of the δD composition of seawater exists, the δD of the seawater in any grid cell has been set equal to the related $\delta^{18}O$ composition, multiplied by a factor of 8, in accordance with the observed relation for meteoric water on a global scale (Craig, 1961). The ECHAM6-wiso simulation is described in detail and evaluated by Cauquoin and Werner (2021). ECHAM6-wiso outputs are given at a 6-hourly resolution. As for the LMDZ-iso model, Amsterdam Island (58 km^2) is too small to be represented by ECHAM6-wiso.

3. Results

3.1 Data description

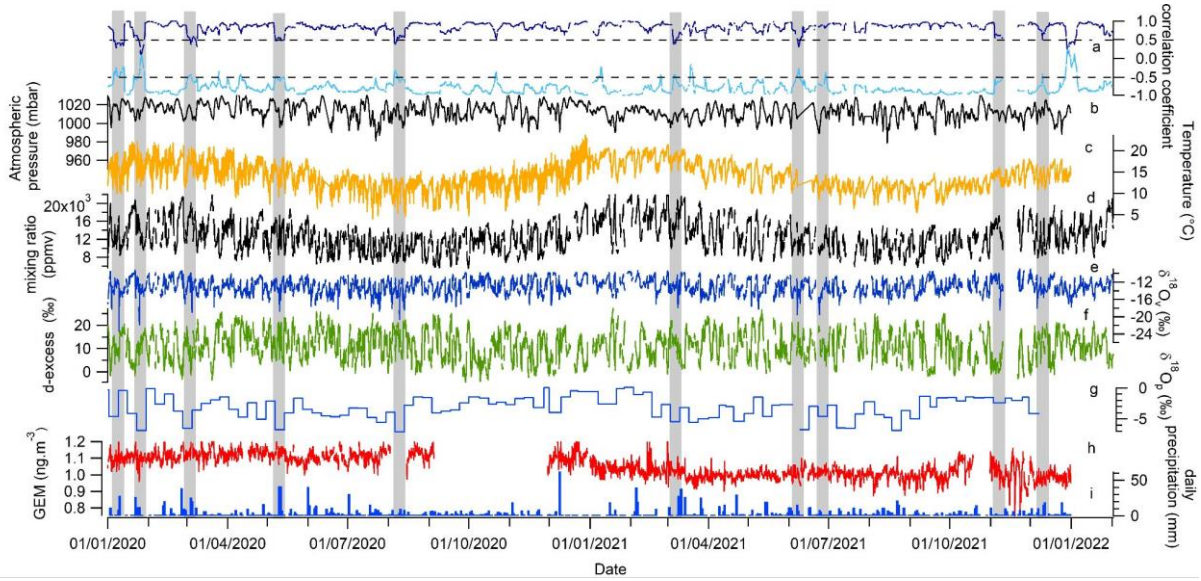

Figure 3 : Meteorological, isotopic and GEM records for the years 2020 and 2021 on the Amsterdam Island : (a) correlation coefficient between $\delta^{18}O_v$ and mixing ratio (dark blue, top) and between $\delta^{18}O_v$ and d-excess$_v$ (light blue, bottom) over a moving time window of 8 days, (b) atmospheric pressure (hourly average), (c) atmospheric temperature (hourly average), (d) water vapor mixing ratio (hourly average), (e) $\delta^{18}O_v$ (hourly average), (f) d-excess$_v$ (hourly average), (g) $\delta^{18}O$ of precipitation sampled on a weekly basis, (h) GEM concentration (hourly average), (i) daily precipitation. The grey shaded areas indicate the ~~the~~ negative excursions in $\delta^{18}O_v$ associated with decorrelation between water vapor mixing ratio and $\delta^{18}O_v$ and a correlation coefficient >-0.5 between d-excess$_v$ and $\delta^{18}O_v$.

3.1.1 Temporal variability in the meteorological records

As mentioned earlier, there is a clear annual cycle at Amsterdam Island as recorded in the temperature and water vapor mixing ratio for the years 2020 and 2021. The December-February period (austral summer) has the highest temperatures with an average of 15.0°C, while in winter (July-September) the average temperature varies around 10.5°C. In parallel, we do not see clear patterns of a diurnal cycle in the temperature record except for some periods yet with a small amplitude (4-5 °C).

The impact of synoptic events at the scale of a few days is visible in the temperature and water mixing ratio with a covariation of temperature and water vapor mixing ratio and amplitudes of up to 10°C and more than 10,000 ppmv.

3.1.2 Temporal variability in the GEM record

Previous studies clearly showed that AMS is little influenced by anthropogenic sources of mercury, and greatly influenced by the ocean surrounding the island (Angot et al., 2014; Hoang et al., 2023; Jiskra et al., 2018; Li et al., 2023; Slemr et al., 2015, 2020). Angot et al., 2014 reported mean annual GEM concentrations of about 1.03 ± 0.08 ng m^{-3} from 2012 to 2013. These concentrations are ~30% lower than those measured at remote sites of the northern hemisphere. Over the period 2012 to 2017, Slmer et al. (2020) confirmed that higher GEM concentrations can be found during austral winter. Lower GEM values are generally observed in October and November, as well as in January and February during austral summer. Using this 6-year long data set, mean annual GEM concentration is 1.04 ± 0.07 ng m^{-3} (annual range: 1.014 to 1.080 ng m^{-3}) i.e. very close to the one observed by Angot et al. (2014).

Surprisingly, unlike the 2012-2017 data set, GEM presented in this study did not show a significant higher mean concentration during the austral winter months than during the summer months (Figure 3), with consequently no discernible seasonal amplitude of GEM. On a finer timescale, the lack of a clear pattern of GEM seasonal cycle is counterbalanced by days showing abrupt increases or decreases in concentrations. Some of the sudden GEM decreases appear concomitant with important negative peaks of several ‰ in $\delta^{18}O_v$.

3.1.3 Temporal variability of water isotopic composition

The isotopic composition of precipitation ($\delta^{18}O_p$) sampled on a weekly basis displays a quite large variability ($\delta^{18}O_p$ = -3.06 ± 1.75 ‰, n=104) with values slightly higher during austral summer (difference between summer and winter $\delta^{18}O_p$ values is about 2 to 3 ‰) (Figure 3). No

significant seasonal variations are observed in the record of d-excess of precipitation (not shown).

No diurnal cycle can be detected in the $\delta^{18}O_v$ and d-excess$_v$. An annual cycle is not visible either (1 ‰ difference between summer and winter mean $\delta^{18}O_v$ value while standard deviation of the entire record at 1 h resolution is 1.7 ‰). Only the synoptic scale variability is well expressed in the records of $\delta^{18}O_v$ and d-excess$_v$ with an anticorrelation between both parameters when looking at the 2-year series at hourly resolution (R^2 = 0.61 with R^2 being the coefficient of determination for a linear regression). Moreover, $\delta^{18}O_v$ is most of the time correlated with water vapor mixing ratio (R^2 = 0.55 for the 2-year series at hourly resolution).

There are a few exceptions to the general correlation between water vapor $\delta^{18}O$ and water vapor mixing ratio as illustrated in Figure 3. Short periods of a few days are associated with a decrease of the correlation coefficient, R estimated from the correlation between $\delta^{18}O_v$ and q_v (R is calculated continuously from hourly records on an 8-day moving window). The periods of low R are also often characterized by a negative peak of several ‰ in $\delta^{18}O_v$, which is not visible in the d-excess$_v$. During these $\delta^{18}O_v$ excursions, the general anti-correlation between $\delta^{18}O_v$ and d-excess$_v$ hence also breaks down. Our study mostly focuses on the 11 most prominent abrupt events highlighted in the -$\delta^{18}O_v$ record (only 10 visible on Figure 3 because of the scale). The 11 most abrupt events occurring when correlation coefficient R between $\delta^{18}O_v$ and d-excess$_v$ is larger than -0.5 are associated with $\delta^{18}O_v$ negative excursion larger than 3 ‰ (at 6h resolution) over a period of less than 24 h, the length of the event being measured between the mid-slopes of the decrease and subsequent increase of the $\delta^{18}O_v$. The 11 selected negative excursions occur at a rate larger than -0.5‰ h^{-1} and the $\delta^{18}O_v$ increase at the end of each excursion has an amplitude larger than half the amplitude of the corresponding initial decrease.

3.2 Model-data comparison

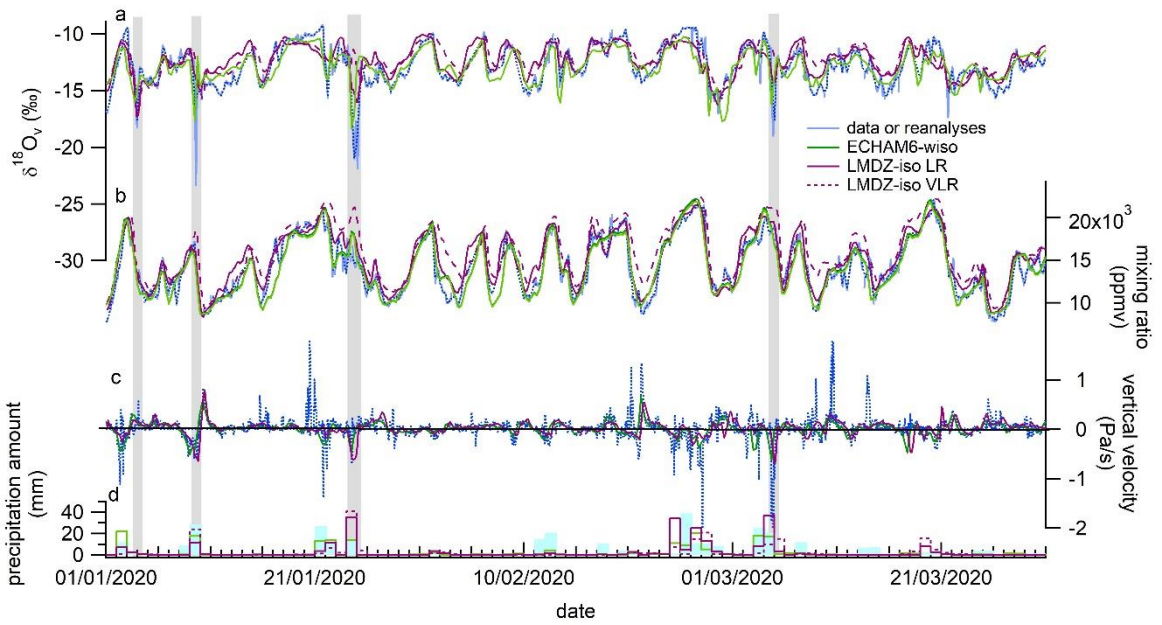

Figure 4: Model-measurement comparison (January – March 2020); a- $\delta^{18}O_v$ (light blue for data on hourly average, dotted dark blue for data resampled at a 6-hour resolution); b- water vapor mixing ratio from our data set; c- vertical velocity; d- Precipitation amount. The grey shaded areas highlight the negative $\delta^{18}O_v$ excursions as defined in 3.1.3 (note that in this figure the excursions of the 3rd and 9th of January 2020 are distinct while the distinction could not be done on Figure 3 because of the scale).

We selected a 3-month period (January to March 2020) for the comparison between our dataset and the outputs of the ECHAM6-wiso and LMDZ-iso models. This period has been selected for display because it encompasses 4 out the 11 negative excursions of $\delta^{18}O_v$, but the extended comparison over the whole 2 years period is displayed in Figure A1. There is an overall agreement between the measured and modelled $\delta^{18}O_v$ and water vapor mixing ratio (Figure 4). The best agreement over the 3-month series is obtained with the ECHAM6-wiso and LMDZ-iso (LR) models (R^2 = 0.59 – 0.6 and 0.87 - 0.90 respectively for $\delta^{18}O_v$ and water vapor mixing ratio series) while a slightly less good agreement is observed with the VLR simulation of the LMDZ-iso model (R^2 = 0.49 and 0.79 respectively for $\delta^{18}O_v$ and water vapor mixing ratio series). The same observation can be done on the entire 2-year time series. We also compare the precipitation amount modelled by ECHAM6-wiso and LMDZ-iso to the precipitation amount measured by the MeteoFrance weather station. The correlation between modeled and measured precipitation is close to zero for LMDZ-iso (R^2 = 0.08 – 0.13 for VLR - LR) while there is a better agreement when comparing measured precipitation amount to outputs of

ECHAM6-wiso (R^2 = 0.45). Finally, when focusing on the short term negative $\delta^{18}O_v$ excursions (Figures 4 and A1), they are in general more strongly expressed in the measurement time series than in the model series. Part of this disagreement can be explained by the fact that the $\delta^{18}O_v$ record has a higher temporal resolution (1h) than the model outputs (3h for LMDZ-iso and 6h for ECHAM6-wiso). However, when interpolating the $\delta^{18}O_v$ record at a 6h resolution (dotted dark blue), the negative excursions are still clearly visible while not captured by the LMDZ-iso model (Figure 4 and Table 1). When looking at the whole 2-year series, the LMDZ-iso VLR simulation fails to reproduce most of these $\delta^{18}O_v$ excursions (only the negative excursion of 3rd January, 2020 is reproduced) while the ECHAM6-wiso model is able to capture all the $\delta^{18}O_v$ excursions. The LMDZ-iso LR simulation produces a negative $\delta^{18}O_v$ excursion over many events with a significantly lesser amplitude than in the data and in the ECHAM6-wiso model (Table 1).

4. Discussion

The most remarkable pattern from this 2-year series is the succession of short negative excursions of $\delta^{18}O_v$ associated with decorrelation between $\delta^{18}O_v$ and humidity, $\delta^{18}O_v$ and d-excess$_v$, and which are highlighted with grey shaded areas in Figure 3, detailed in Figures 5 and A2 and referenced in Table 1. These negative $\delta^{18}O_v$ excursions always occurred during low pressure periods (atmospheric pressure below 1005 mbar) and we observe the presence of a cold front within a distance of 100 km around Amsterdam Island in a 48h period covering the time of the event (Ssupplementary Mmaterial Figure S1). The focus on the first three months of the series presented in Figure 4 shows that these events are captured by ECHAM6-wiso at 0.9° resolution, but not systematically by LMDZ-iso at 2x1.67° and even less by LMDZ-iso at 3.75x1.9° resolution. Such mismatch makes the understanding of the processes at play during these events particularly important to investigate to further improve the performances of atmospheric general circulation models equipped with water isotopes. .

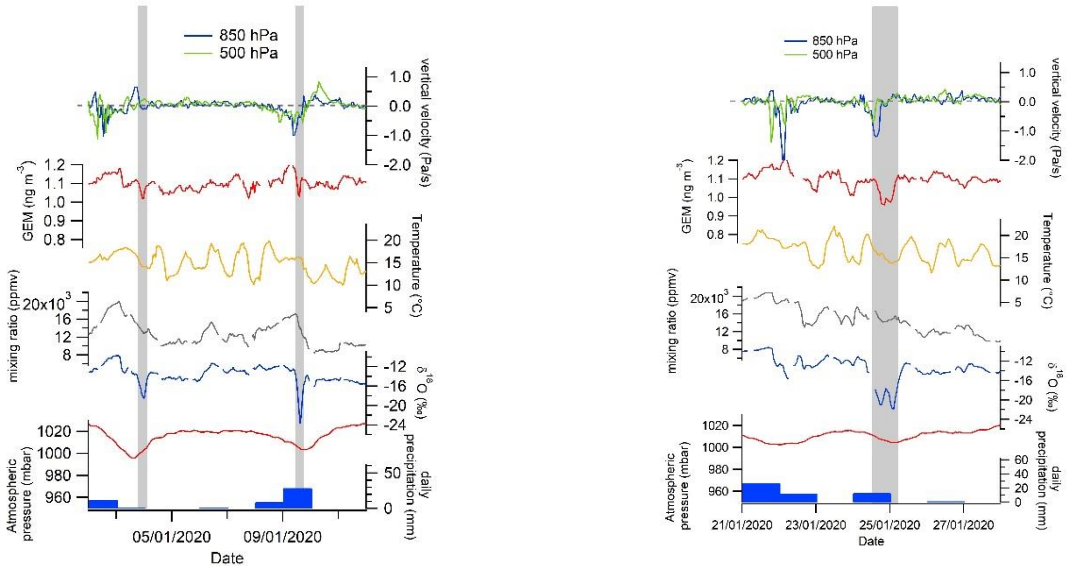

Figure 5: Evolution of GEM, $\delta^{18}O_v$, water vapor mixing ratio, meteorological parameters (surface temperature, surface atmospheric pressure, daily precipitation) measured by the MeteoFrance weather station and vertical velocity from the ERA5 reanalyses at 500 and 850 hPa over the three isotopic excursions of January 2020 identified on Figure 4. A focus on the other excursions is provided in Figure A2.

Table 1: List of the 11 events associated with both loss of correlation between $\delta^{18}O_v$ and q_v, $\delta^{18}O_v$ and d-excess$_v$ and negative excursions of $\delta^{18}O_v$ over 2020-2021. The amplitude of the negative $\delta^{18}O_v$ anomaly is calculated from ~~–~~the minimum of $\delta^{18}O_v$ on the record at hourly resolution (at 6h resolution). ~~.~~When the calculated amplitude is smaller than 1 ‰, we indicate only "-". When the vertical velocity is between -0.25 and 0.25 Pa/s, ~~we~~ this is indicated in the table as "~0".

Date of the event	Negative excursion of GEM	Low pressure (< 1005 mbar)	Rain	Relative Humidity at the surface (at minimum $\delta^{18}O_v$)	vertical velocity from reanalyses (850 hPa)	vertical velocity from reanalyses (500 hPa)	Length of the event (hours)	amplitude of the $\delta^{18}O_v$ peak in the data (‰)	amplitude of the $\delta^{18}O$ peak in ECHAM-wiso (‰)	amplitude of the $\delta^{18}O$ peak in LMDZ-iso VLR (‰)	amplitude of the $\delta^{18}O$ peak in LMDZ-iso LR (‰)
06/12/2021	Yes	Yes	Yes	82%	~0	up	3h	-6 (-5)	-2.3	-	-2
08/11/2021	Yes	Yes	No	85%	~0	~0	17h	-5.5 (-5.5)	-5	-	-4
23/06/2021	No	Yes	Yes	75%	~0	~0	10h	-5.5 (-5.4)	-6	-	-
07/06/2021	No	Yes	Yes	80%	up	~0	9h	-6.5 (-5.8)	-5.8	-	-2
08/03/2021	Yes	Yes	Yes	89%	down	up	20h	-6 (-6)	-4	-	-
09/08/2020	No data	Yes	Yes	87%	down	up	8h	-8 (-6)	-7	-	-2
10/05/2020	Small	Yes	Yes	95%	down	down	14h	-4.9 (-4)	-3	-	-3
04/03/2020	No data	Yes	Yes	98%	up	up	9h	-6.1 (-5.3)	-5	-	-
24/01/2020 (double peak)	Yes	Yes	Yes	93% and 90%	1st peak up and 2nd peak down	1st peak up and 2nd peak down	17h	-7.8 (-7.5)	-4.5	-	-3.5
09/01/2020	Yes	Yes	Yes	94%	up	up	4h	-9 (-4)	-5	-	-
03/01/2020	Yes	Yes	No	90%	down	~0	6h	-2.8 (-2.5)	-2.4	-3	-3.5

Several hypotheses can be proposed to explain the negative excursions of $\delta^{18}O_v$. The beginning of these excursions is associated with a decrease of the water vapor mixing ratio and occurs in most cases during a precipitation event (Table 1). These events share similarities with negative $\delta^{18}O_v$ and $\delta^{18}O_p$ short events previously observed in temperate regions during a cold front passage (e.g. Aemisegger et al., 2015). Three possible processes at play to explain such events have already been listed in previous studies (e.g. Dütsch et al., 2016) (i) local interaction between the vapor and the rain droplets (rain equilibration and rain evaporation), (ii) vertical subsidence of water vapor with depleted isotopic composition, or (iii) horizontal advection through the arrival of a cold front. We explore below how we can gain information on the different processes using our data set, back trajectories and model-data comparison.

4.1 $\delta^{18}O_v$ vs q_v relationship

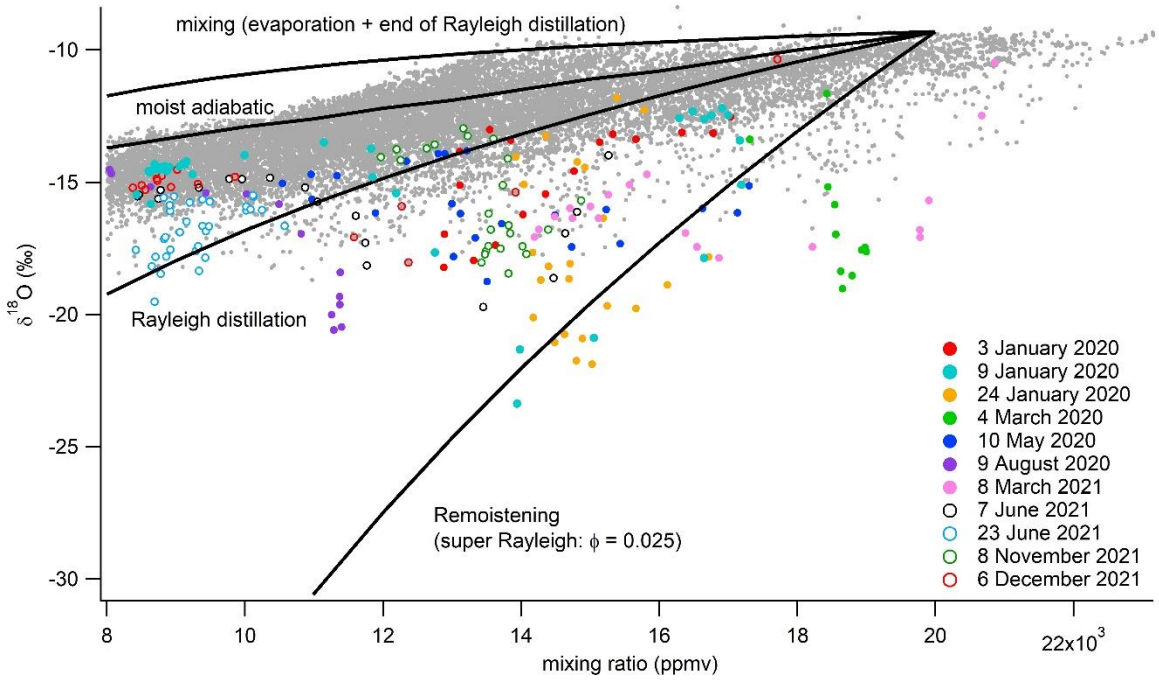

Figure 6: Relative evolution of q_v and $\delta^{18}O_v$ for the different events (colors according to the date as explained in the graph) and for the entire 2 years records (grey). The solid lines are theoretical lines whose equations are detailed in Noone (2012) for different processes (remoistening associated with exchange between rain and water vapor; Rayleigh distillation assuming that all formed condensation is removed from the cloud; moist adiabatic process assuming that liquid condensation stays in the cloud with the water vapor; mixing of water vapor from ocean evaporation around Amsterdam Island and water vapor from the end of the Rayleigh distillation, i.e. high altitude water vapor). The water vapor for the calculation of Rayleigh distillation and for the evaporation above the ocean has a $q_{v,0}$ of 20,000 ppmv and a $\delta^{18}O_{v,0}$ of -9.3 ‰. The vapor at the end of the distillation line ~~was taken with~~has a water vapor mixing ratio of 1,000 ppmv and a $\delta^{18}O_v$ of -40 ‰.

First, to test the hypothesis of vapor-droplet interactions, we looked at the $\delta^{18}O_v$ vs q_v distribution following the approach already used by Guilpart et al. (2017) (Figure 6). We acknowledge that our approach is crude and should be taken as a first order approach since we can only look at the water vapor $\delta^{18}O_v$ vs q_v distribution in the surface layer using adapted boundary conditions while it may be more relevant to look at this relationship in the free troposphere. In general, the $\delta^{18}O_v$ vs q_v evolution lies on a curve which can be explained by condensation processes (Rayleigh distillation or reversible moist adiabatic process). However,

for the 11 events highlighted above, the water vapor $\delta^{18}O_v$ vs q_v evolution follows an evolution standing below the curve of the $\delta^{18}O_v$ vs q_v evolution observed for the rest of the series. ~~Even~~ Although the evolution of~~if~~ the water vapor $\delta^{18}O_v$ vs q_v ~~evolution~~ is rather abrupt~~steep~~, there is a certain~~some~~ resemblance with the idealized theoretical remoistening curve ~~for remoistening~~ initially calculated for the free troposphere (Noone, 2012) and adapted here with initial conditions corresponding to the isotopic composition of surface water vapor~~ isotopic composition.~~ . Remoistening is described through a modification of the equilibrium fractionation coefficient between water vapor and rain (α_e) so that the effective fractionation factor is $\alpha=(1+\phi)\times\alpha_e$, ϕ being the degree to which α deviates from equilibrium. This effective fractionation coefficient is then introduced in the Rayleigh distillation equation to deduce the link between $\delta^{18}O_v$ and mixing ratio as:

$$\delta^{18}O_v - \delta^{18}O_{v,0} = (\alpha-1)\times\ln(q_v/q_{v,0}) \qquad \text{(Eq 8)}$$

Despite the simplicity of our approach, the fact that the water vapor $\delta^{18}O_v$ vs q_v evolution lies below the idealized curve for condensation processes supports the depleting effect of vapor-rain interactions for our negative water vapor $\delta^{18}O_v$ excursions (Noone, 2012; Worden et al., 2007). Surface relative humidity remains relatively high during these events (values given in Table 1 compared to a mean value of 77 %) which favors rain-vapor diffusive exchanges. ~~Such~~ This interpretation is also supported by the stable d-excess$_v$ during these events.

4.2 $\delta^{18}O_v$ vs GEM relationship

Second, to test the hypothesis of subsidence of air from higher altitude, GEM is used. Indeed, aircraft measurements as well as model simulations demonstrated that the upper troposphere/lower stratosphere is depleted in GEM and enriched in species composed of reactive gaseous mercury and particulate bound mercury (Lyman and Jaffe, 2012; Murphy et al., 2006; Sillman et al., 2007; Swartzendruber et al., 2006, 2008; Talbot et al., 2007, 2008). This leads to lower GEM concentrations than those usually observed when the lowest atmosphere layer is only under marine influence (Angot et al., 2014; Lindberg et al., 2007). The fact that GEM negative excursions are observed in phase with negative $\delta^{18}O_v$ excursions in most of the events (6 events on a total of 9 events with GEM data, cf Figure 5 and A2, Table 1) suggests that vertical subsidence of water vapor, $\delta^{18}O$-depleted by Rayleigh distillation and/or rain-vapor interactions, can have an influence on the observed excursions of $\delta^{18}O_v$, in agreement with the conclusion of Dütsch et al. (2016).

4.3 Back trajectories information

To further explore the processes leading to the decoupling of humidity and $\delta^{18}O_v$ as well as sharp negative excursions of $\delta^{18}O_v$ during the 11 events identified here, we also use information from the ERA5 reanalyses. In particular, the influence of atmospheric circulation (vertical and horizontal advection) and moisture origin can be studied through back trajectories. The back trajectories, presented here for 3 events (Figures 7, A3 and A4), confirm the information from wind directions that there is no systematic change in the horizontal origin of the trajectories for the different events. No systematic pattern is identified either in the vertical advection even if we note that for the event of January 3rd, the average altitude of the envelope of the 5-day back trajectories increases when comparing the situation before the excursion and the situation when the most negative $\delta^{18}O_v$ values are reached. This observation may support the occurrence of air subsidence as indicated by the GEM record for this particular event (Figure 5).

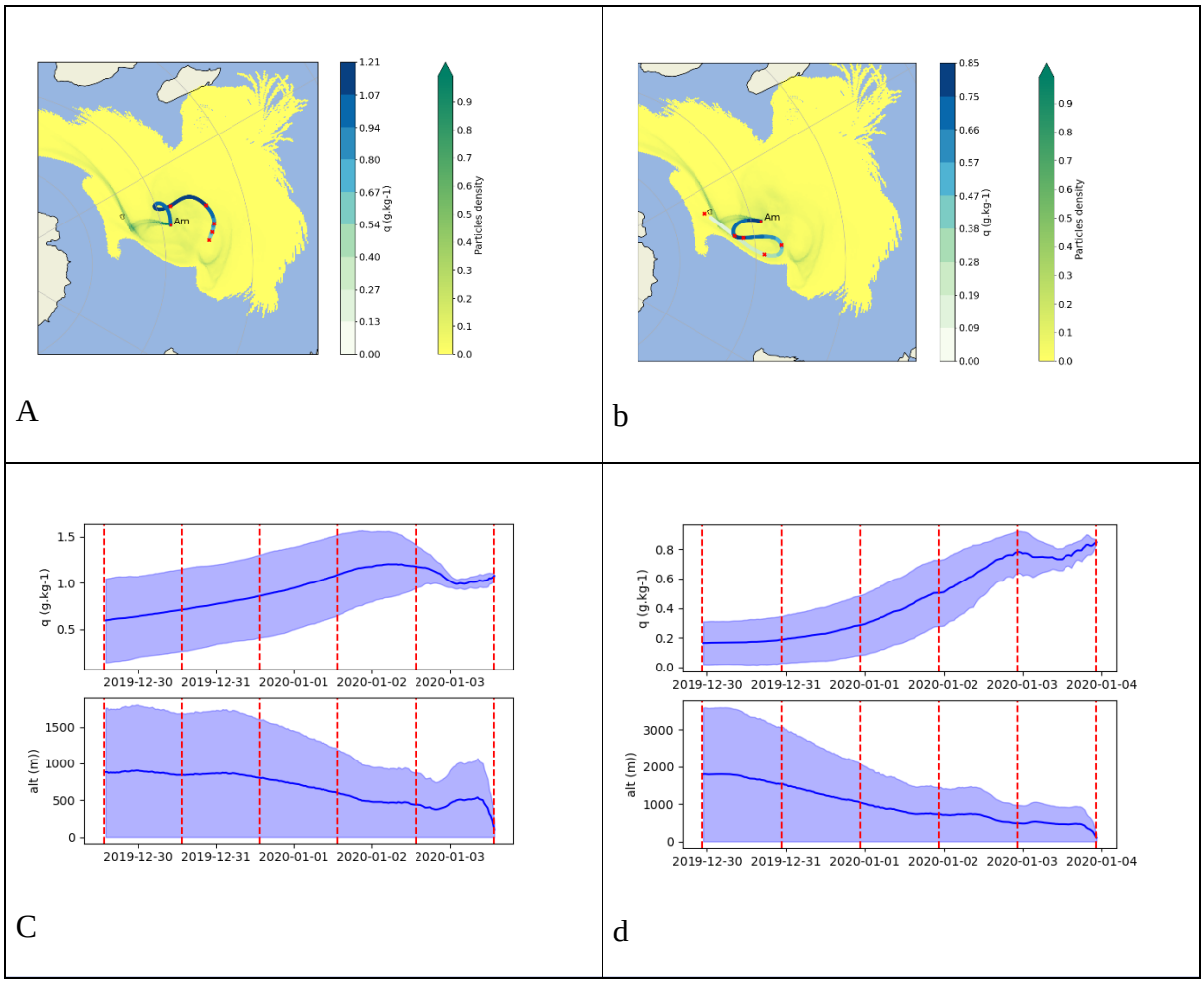

Figure 7 : FLEXPART footprints of 5-day back trajectories for the event of the 3rd-4th of January. (a) Latitude-longitude projection of the FLEXPART back trajectory footprints for

January 3rd 2020 at 13h30. The yellow to green colors on each grid point of these projections represent the density of particles. The white to blue colors indicate the water vapor mixing ratio along the humidity-weighted average back trajectory. Each red point indicates the location of the average back trajectory for each of the 5 days before the date of the considered event. (b) Same as a for January 3rd 2020 at 22h30. (c) Top shows the evolution of the water vapor mixing ratio of the back trajectories for January 3rd 2020 at 13h30; bottom shows the altitude evolution of the back trajectory for January 3rd 2020 at 13h30. (d) same as (c) for January 3rd 2020 at 22h30.

The subsidence over the different events can better be studied from the vertical velocity from the ERA5 reanalyses (Figure 4 and A1). Subsidence (positive vertical velocity) is not systematically associated with negative $\delta^{18}O_v$ excursions: subsidence at either 850 hPa or 500 hPa is observed only for 5 events over 11 (Table 1). In 4 cases, there is rather an ascending movement of the atmospheric air associated with the rain event. In the other cases, there is no clear vertical movement. However, we note that when negative $\delta^{18}O_v$ excursions are not concomitant with subsidence, they occur ~~right after an ascending movement and are generally followed by subsidence~~at the end of an ascending movement which is generally followed by subsidence (Figures A1 and A2).

4.4 Model – data comparison and atmospheric dynamic

With the information gathered above, both subsidence and isotopic depletion associated with rain occurrence and further interaction between droplets and water vapor can explain the negative excursions of $\delta^{18}O_v$. We note however that the data gathered so far do not permit to provide a simple and unique explanation. Neither subsidence nor rain systematically occurred for each of the $\delta^{18}O_v$ excursion. Still, the fact that at least ECHAM6-wiso is able to reproduce every negative $\delta^{18}O_v$ excursion (whether they are associated or not with subsidence or rain-water vapor reequilibration) shows that ~~not only~~(1) the patterns of atmospheric water cycle are correctly reproduced, ~~(~~a validation which can ~~also~~ be performed using humidity and precipitation data for some aspects but benefits from water isotopes implementation for the residence time of water)and (2) ~~but also that~~ the isotopic processes are correctly implemented in this model. Such abrupt $\delta^{18}O_v$ events can hence be used as a test bed of the performances of water isotopes enabled general circulation models.

To further explore the $\delta^{18}O_v$ data-model comparison and associated processes, we compare the performances of the ECHAM6-wiso and the LMDZ-iso models over the first months of 2020 in terms of atmospheric dynamics (Figures 4 and A1). First and as expected because of the nudging, the two models reproduce rather well the evolution of the vertical velocity of the ERA5 reanalyses with a stronger ascent for the model predicting the strongest precipitation amount (e.g. LMDZ-iso for January 24th 2020). The event of January 3rd is the only one reproduced by both ECHAM6-wiso and the two versions of the LMDZ-iso model: the three simulations show a clear subsidence over the isotopic event and a clear negative $\delta^{18}O_v$ excursion. For the other events, neither LMDZ-iso nor ECHAM6-wiso show a clear signal of subsidence neither at 500 nor at 850 hPa (not shown~~Figures 4 and A1~~). However, the horizontal distribution of vertical velocity obtained with ECHAM6-wiso and LMDZ-iso are significantly different (Figure 8 for the event of the 9th of January, S~~s~~upplementary M~~m~~aterial Figures S2 and S3 for the other events). While the LMDZ-iso modelled vertical velocity displays a rather strong homogeneity on the vertical axis, ECHAM6-wiso modelled vertical velocity highlights subsidence of air below the ascending column, ~~at the exact location of the negative $\delta^{18}O_v$ anomaly~~ with the maximum of negative $\delta^{18}O_v$ anomaly at the surface located just at the limit between ascendance and subsidence (between 75°E and 77°E in Figure 8c). This subsidence of depleted $\delta^{18}O_v$ below the ascending column is responsible for the sharp negative $\delta^{18}O_v$ excursion in the ECHAM6-wiso model. The fact that subsidence of air occurs just below uplifted air, at the limit between ascendance and subsidence (Figure 8k~~j~~ and Supplementary Material Figure S2~~4~~), permits to reconcile the GEM data suggesting subsidence and the sign of the vertical velocity of the ERA5 reanalyses at Amsterdam Island suggesting that many excursions start with ascendance. Since the isotope implementation was done similarly in the two models, the reason why the LMDZ-iso model does not reproduce the water isotopic anomaly is its too coarse resolution as also supported by the comparison between performances of the LMDZ-iso model at low resolution and very low resolution for the event of the 24th of January (Table 1 and Figure 4). As already pointed by Ryan et al. (2000), a fine resolution is necessary to correctly simulate front dynamics and we extend this result here to the high resolution temporal patterns of surface $\delta^{18}O_v$.

4.5 Synthesis

Figure 9 summarizes the proposed mechanism for negative $\delta^{18}O_v$ excursions as inferred from our data – model comparison when there is a clear rain event. A rain event is associated with a

strong ascending column in which $\delta^{18}O_v$ is depleted by progressive precipitation during the ascent and by interaction between rain and water vapor. ~~This ascending column is coupled to the subsidence of $\delta^{18}O_v$ depleted air at the rear of the event, which is pushed toward Amsterdam Island through a south west advection of cold air.~~ This ascending column is generally associated with a cold front moving from South-West to North-Est (Fig. 8j and Supplementary Material S1), with subsidence and $\delta^{18}O_v$ depleted air at the rear of the front (Fig. 8 and Supplementary Material S2 and S3).

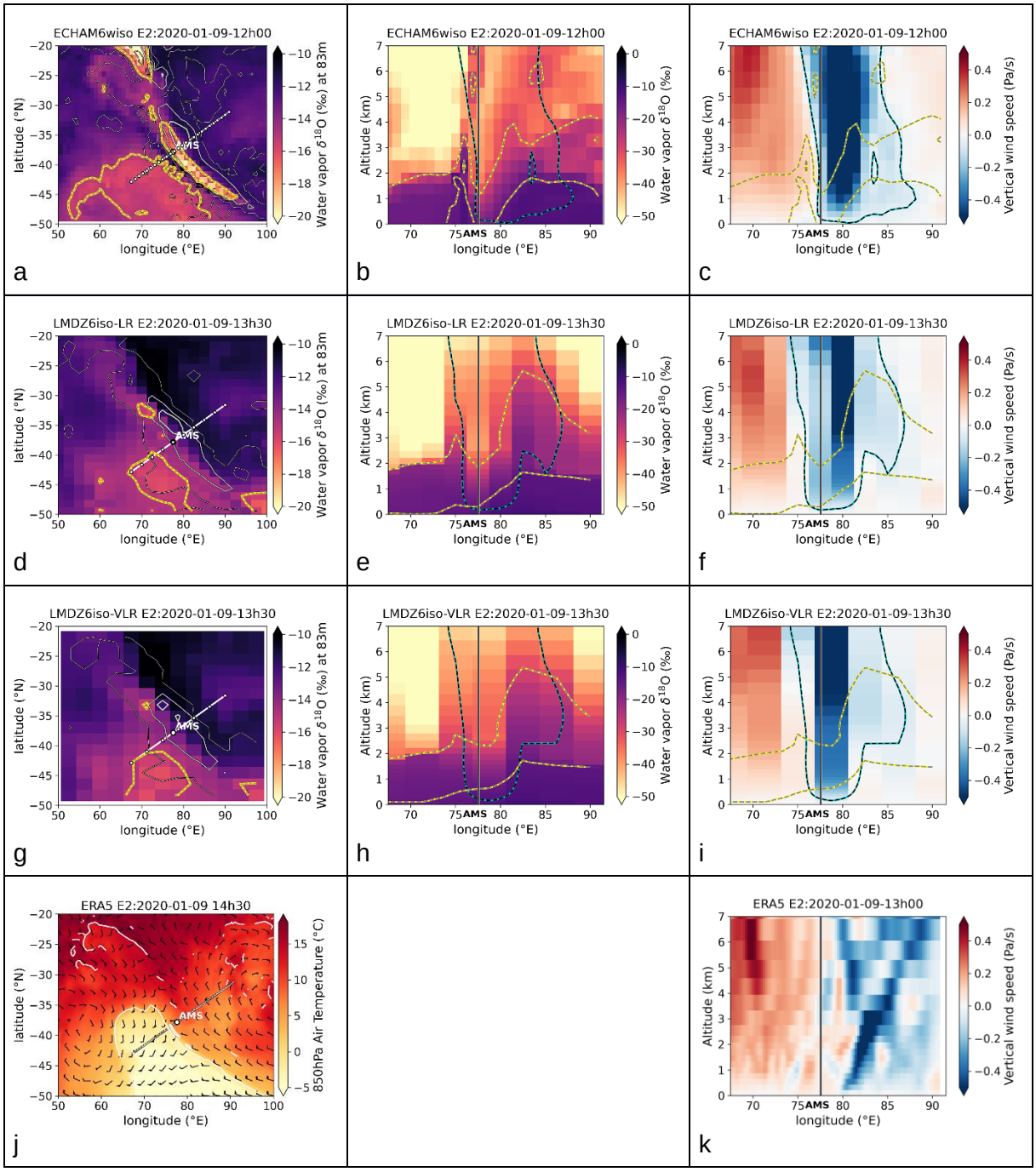

Figure 8: Modelled $\delta^{18}O_v$ and vertical velocity for the event of January 9th 2020. (a) Surface air $\delta^{18}O_v$ (~83 m, latitude vs longitude), with yellow line indicating -15 ‰ contour level and grey lines indicating precipitation contours at 0.5, 10, and 50 mm day^{-1} (thin, medium and thick lines respectively); (b) $\delta^{18}O_v$ plotted on a vertical cross-section (altitude vs longitude) along the transect indicated by the white line on panel (a), with yellow lines indicating $\delta^{18}O_v$ contours at -30 ‰ and -15 ‰, blue lines indicating the contour of –0.05 Pa s^{-1} vertical velocity (ascendance), and the vertical black line denoting the longitude of Amsterdam Island; (c) Vertical velocity plotted on a vertical cross-section as for (b), with same contour lines. (a), (b)

and (c) are drawn using outputs of the ECHAM6-wiso model ; (d), (e) and (f) are the same as (a), (b) and (c) but obtained from the LMDZ-iso model at low resolution (LR) ; (g), (h) and (i) are the same as (a), (b) and (c) but obtained from the LMDZ-iso model at very low resolution (VLR). (j) ERA5 air temperature at 850 hPa, with white lines marking front locations (see Supplementary Material S1); (k) ERA5 vertical velocity plotted on a vertical cross-section (altitude vs longitude) along the transect indicated by the black dotted line on panel (j).

~~Pattern of the modelled $\delta^{18}O_v$ and vertical velocity for the event of January 9th 2020. (a) low level (~83 m) contourplot of $\delta^{18}O_v$ in a latitude vs longitude plot, the yellow line indicates the -15‰ level and grey contours indicate precipitation contours at 0.5, 10, and 50 mm day^{-1} (thin, medium and thick lines respectively); (b) $\delta^{18}O_v$ evolution in an altitude vs longitude plot, the yellow lines indicate the $\delta^{18}O_v$ levels at -30 and -15 ‰, the blue one plots the contour of -0.05 Pa s^{-1} vertical velocity (ascendance) and the vertical black line denotes Amsterdam Island longitude; (c) vertical velocity in an altitude vs longitude plot with similar lines as in (b) ; (a), (b) and (c) are drawn using outputs of the ECHAM6-wiso model ; (d), (e) and (f) are the same as (a), (b) and (c) but obtained from the LMDZ-iso model at low resolution (LR) ; (g), (h) and (i) are the same as (a), (b) and (c) but obtained from the LMDZ-iso model at very low resolution (VLR); (j) shows the vertical velocity in an altitude vs longitude plot from ERA5.~~

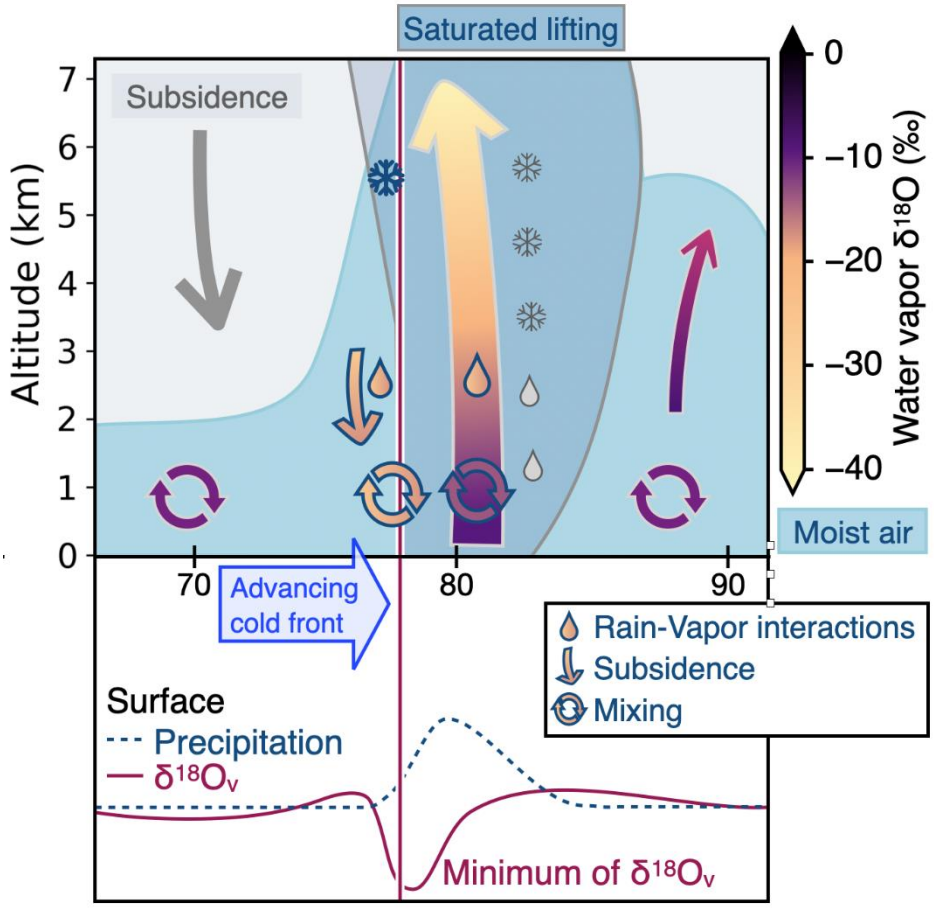

Figure 9: Scheme of the mechanism explaining the sharp negative excursion of $\delta^{18}O_v$ recorded at the surface for cold front events associated with precipitation. The scheme is based on the profile modelled by ECHAM6-wiso for event of January 9th 2020 (see Ssupplementary Mmaterial Figure S5 for other events). The top panel show the altitude vs longitude dynamics of air masses with vertical saturated lifting in the center and subsidence at the rear of the lifting. The bottom panel shows the associated evolution of $\delta^{18}O_v$ and precipitations on the same longitude scale than on the upper panel.

5. Conclusion

We presented here the first water vapor isotopic record over 2 years on Amsterdam Island. The water vapor isotopic variations follow at first order the variations of water vapor mixing ratio as expected for such a marine site. Superimposed to this variability, we have evidenced 11 periods of a few hours characterized by the occurrence of one or two abrupt negative excursions of $\delta^{18}O_v$ while the correlation between $\delta^{18}O_v$ and water vapor mixing ratio does not hold. These negative excursions are often occurring toward the end of precipitation events. They are most

of the time occurring during ~~characterized by~~ a decrease in water vapor mixing ratio. Representation of these short events is a challenge for the atmospheric components of Earth System Models equipped with water isotopes and we found that the ECHAM6-wiso model was able to reproduce most of the sharp negative $\delta^{18}O_v$ excursions while the LMDZ-iso model at low (very low) resolution was only able to reproduce 7 (1) of the negative excursions. The good agreement between modeled and measured $\delta^{18}O_v$ when using ECHAM6-wiso validates the physics processes within the ECHAM6-wiso model as well as the implemented physics of water isotopes.

Using previous modeling studies as well as information provided by (1) the confrontation with other data sources (GEM, meteorology) obtained in parallel on this site, (2) back trajectory analyses and (3) the outputs of the two models ECHAM6-wiso and LMDZ-iso, we conclude that the most plausible explanations for such events are rain-vapor interactions and subsidence at the rear of a precipitation event. Both can be combined, since rain vapor interactions can help maintaining moist conditions in subsidence regions.

This study highlights the added value of combining different data from a surface~~n~~ atmospheric observatory to understand the dynamics of the atmospheric circulation, e.g. subsidence in the higher atmosphere. These 2-year records are also a good benchmark for model evaluation. We have especially shown that the isotopic composition of water vapor measured at the surface is a powerful tool to test the vertical dynamic of atmospheric models and the implementation of water isotopes for those that are equipped with them.~~to identify aspects to be improved in the atmospheric component of the Earth system models.~~ In our case, we used it to test different horizontal resolutions which influence the representativity of the vertical dynamics and have important implication in the simulation of surface variations of water vapor $\delta^{18}O_v$. Our study highlights the importance to have high-resolution models (e.g. mesoscale models) equipped with isotopes to further study such abrupt isotopic events.

Appendices:

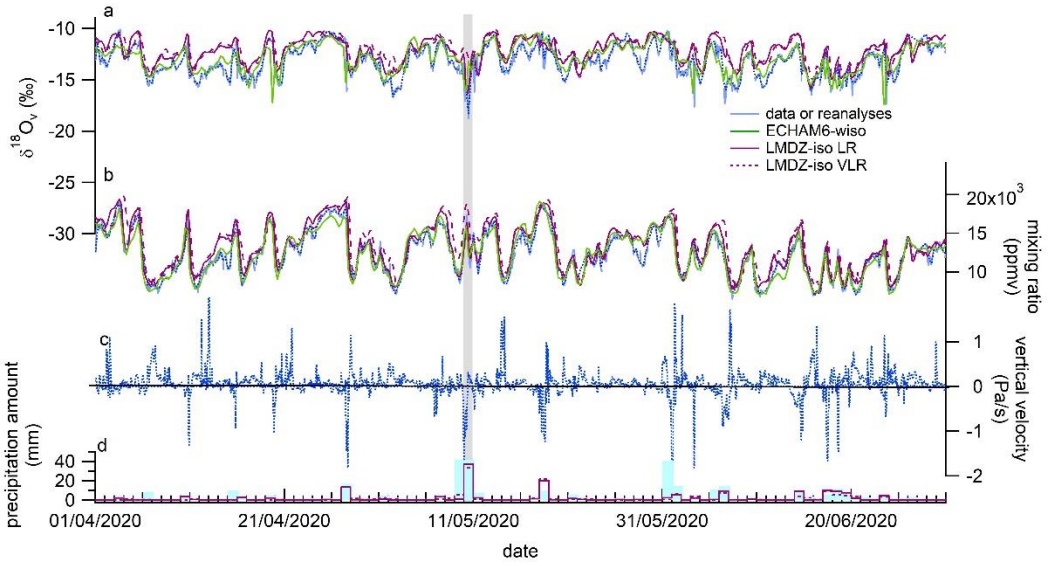
a
b
c
d
-10
-15
-20
-25
-30
δ18Ov (‰)
data or reanalyses
ECHAM6-wiso
LMDZ-iso LR
LMDZ-iso VLR
20x10^3
15
10
mixing ratio (ppmv)
1
0
-1
-2
vertical velocity (Pa/s)
40
20
0
precipitation amount (mm)
01/04/2020
21/04/2020
11/05/2020
31/05/2020
20/06/2020
date

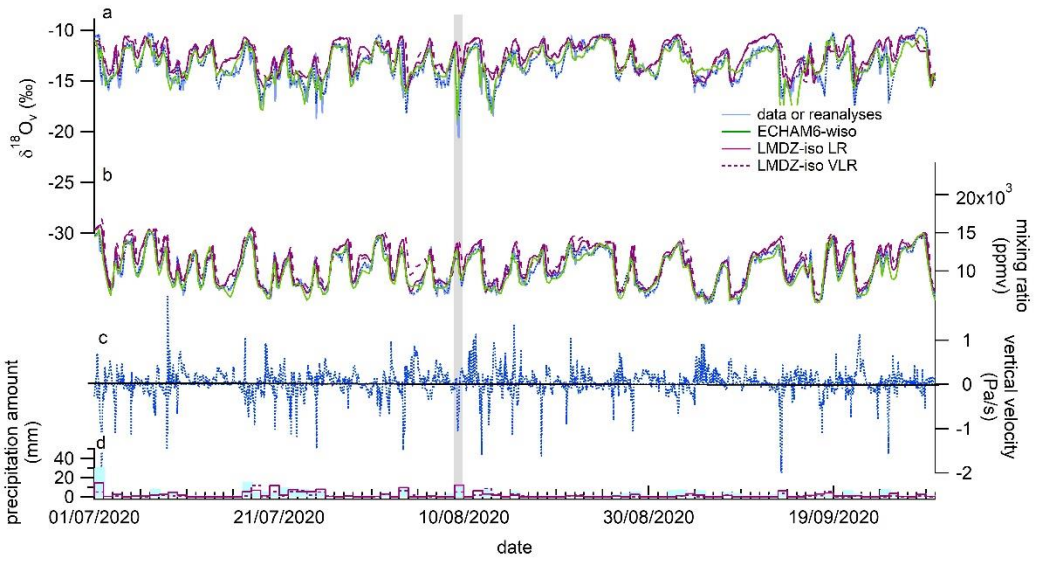
a
b
c
d
-10
-15
-20
-25
-30
δ18Ov (‰)
data or reanalyses
ECHAM6-wiso
LMDZ-iso LR
LMDZ-iso VLR
20x10^3
15
10
mixing ratio (ppmv)
1
0
-1
-2
vertical velocity (Pa/s)
40
20
0
precipitation amount (mm)
01/07/2020
21/07/2020
10/08/2020
30/08/2020
19/09/2020
date

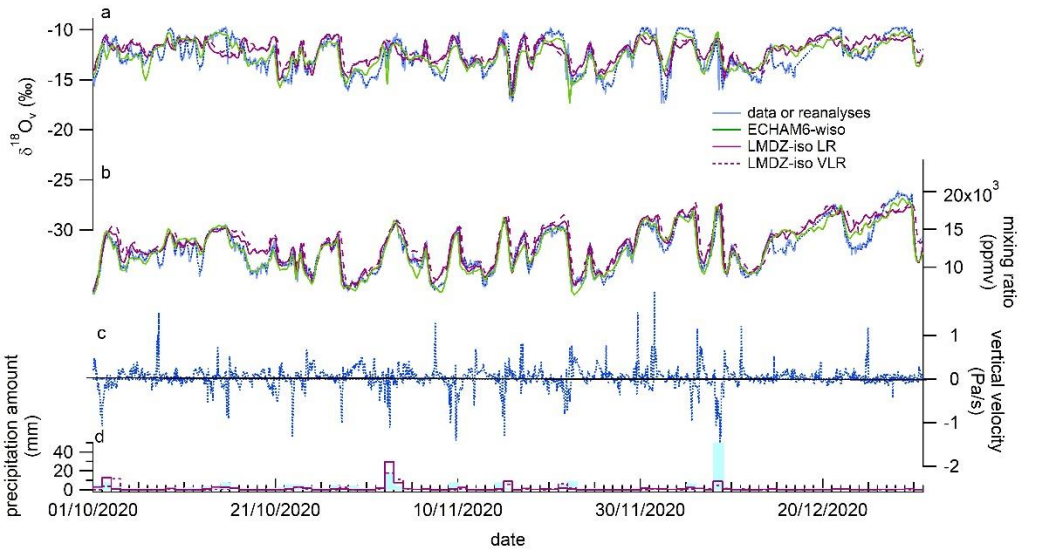
a
b
c
d
-10
-15
-20
-25
-30
δ18Ov (‰)
data or reanalyses
ECHAM6-wiso
LMDZ-iso LR
LMDZ-iso VLR
20x10^3
15
10
mixing ratio (ppmv)
1
0
-1
-2
vertical velocity (Pa/s)
40
20
0
precipitation amount (mm)
01/10/2020
21/10/2020
10/11/2020
30/11/2020
20/12/2020
date

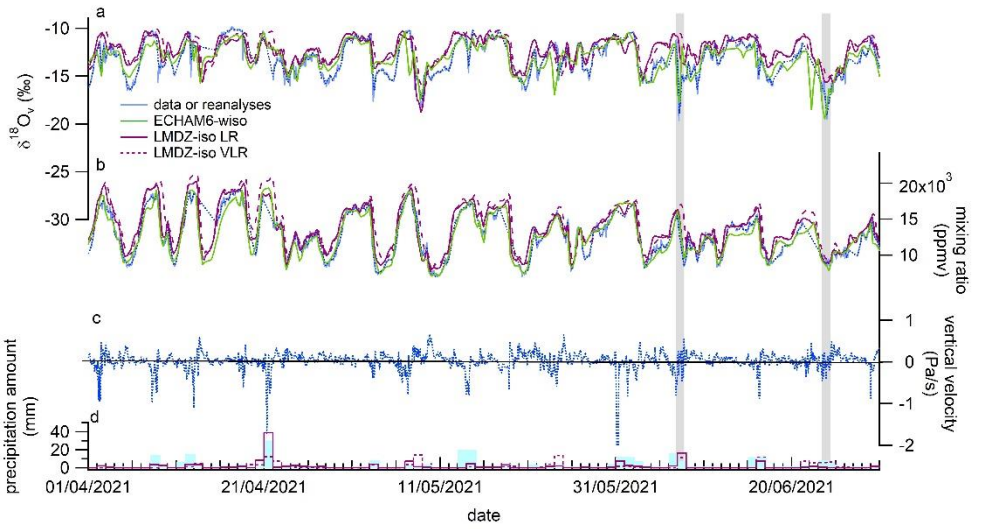
a
b
c
d
data or reanalyses
ECHAM6-wiso
LMDZ-iso LR
LMDZ-iso VLR
δ18Ov (‰)
mixing ratio (ppmv)
vertical velocity (Pa/s)
precipitation amount (mm)
01/04/2021
21/04/2021
11/05/2021
31/05/2021
20/06/2021
date

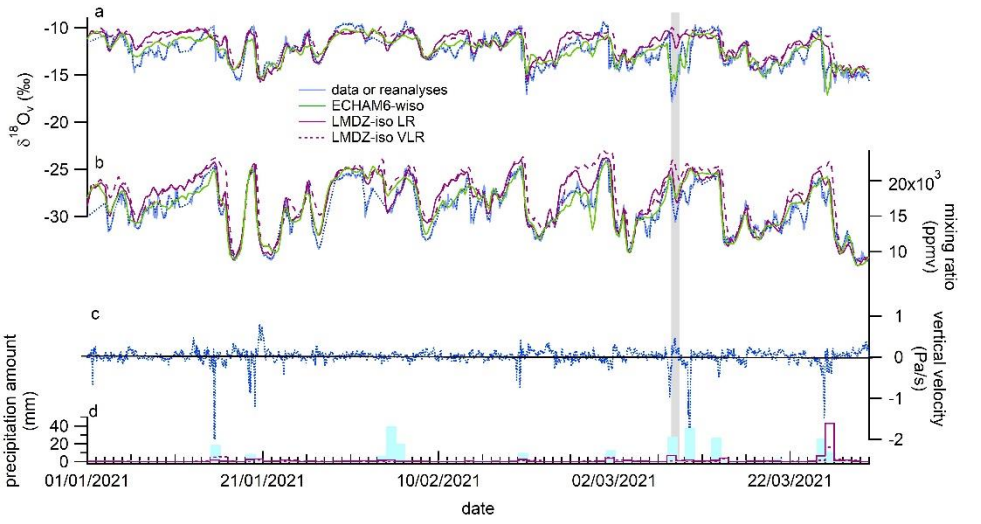
a
b
c
d
data or reanalyses
ECHAM6-wiso
LMDZ-iso LR
LMDZ-iso VLR
δ18Ov (‰)
mixing ratio (ppmv)
vertical velocity (Pa/s)
precipitation amount (mm)
01/01/2021
21/01/2021
10/02/2021
02/03/2021
22/03/2021
date

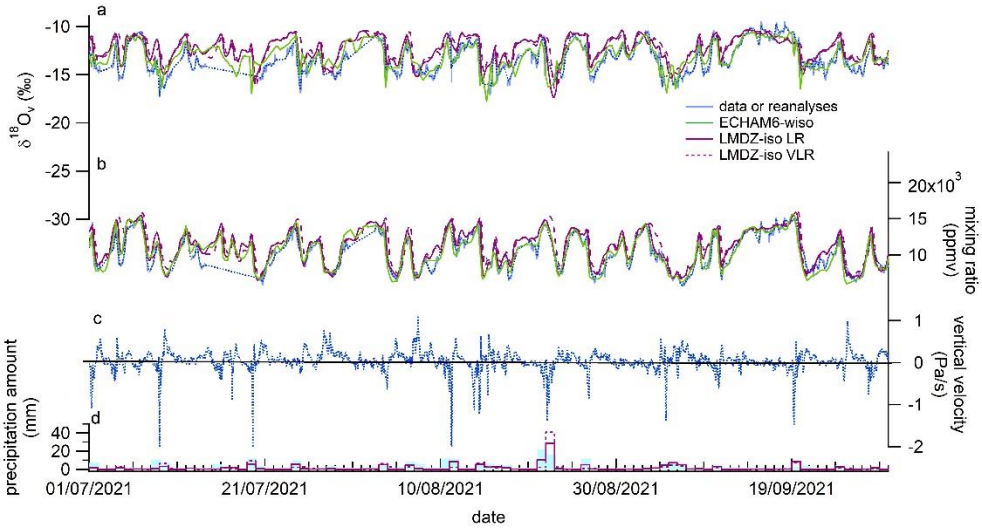
a
b
c
d
data or reanalyses
ECHAM6-wiso
LMDZ-iso LR
LMDZ-iso VLR
δ18Ov (‰)
mixing ratio (ppmv)
vertical velocity (Pa/s)
precipitation amount (mm)
01/07/2021
21/07/2021
10/08/2021
30/08/2021
19/09/2021
date

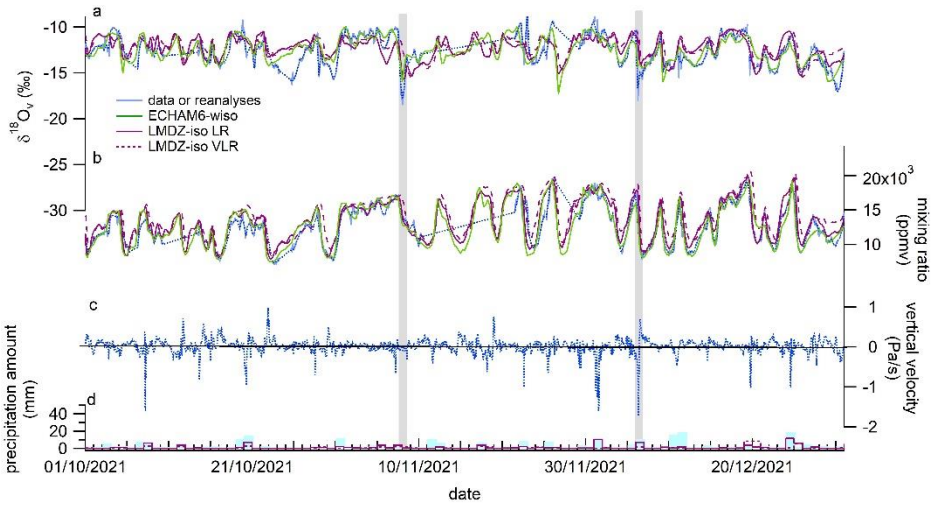

Figure A1: Model-measurement comparison (April 2020 – December 2021); a- $\delta^{18}O_v$ (light blue for data on hourly average, dark blue for data resampled at a 6-hour resolution); b- water vapor mixing ratio from our data set; c- vertical velocity; d- Precipitation amount. The grey shadings highlight the negative $\delta^{18}O_v$ excursions.

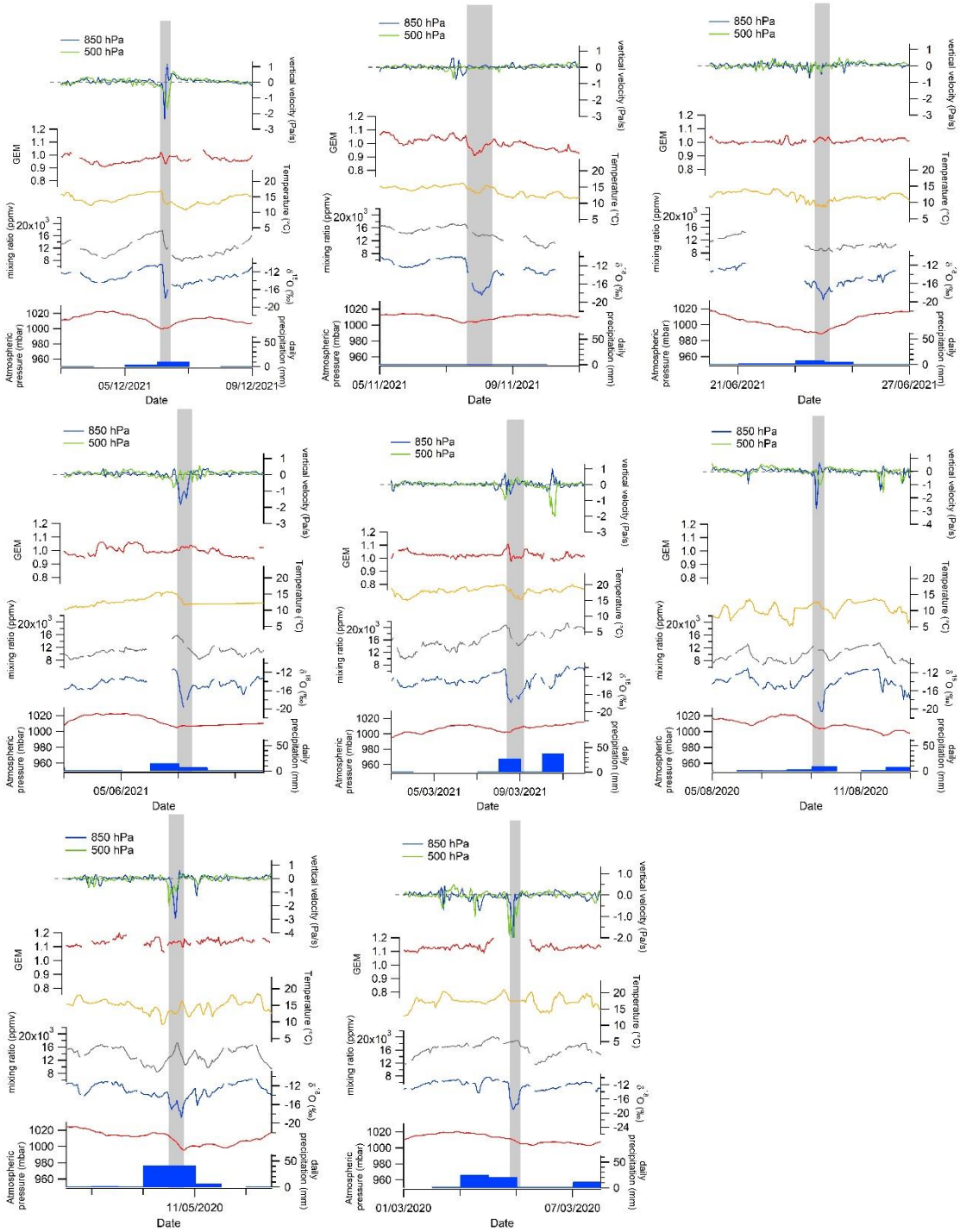

Figure A2 : Evolution of GEM, $\delta^{18}O_v$, water vapor mixing ratio, meteorological parameters (surface temperature, surface atmospheric pressure, daily precipitation) measured by the MeteoFrance weather station and vertical velocity from the ERA5 reanalyses at 500 and 850 hPa over the isotopic excursions between March 2020 and December 2021.

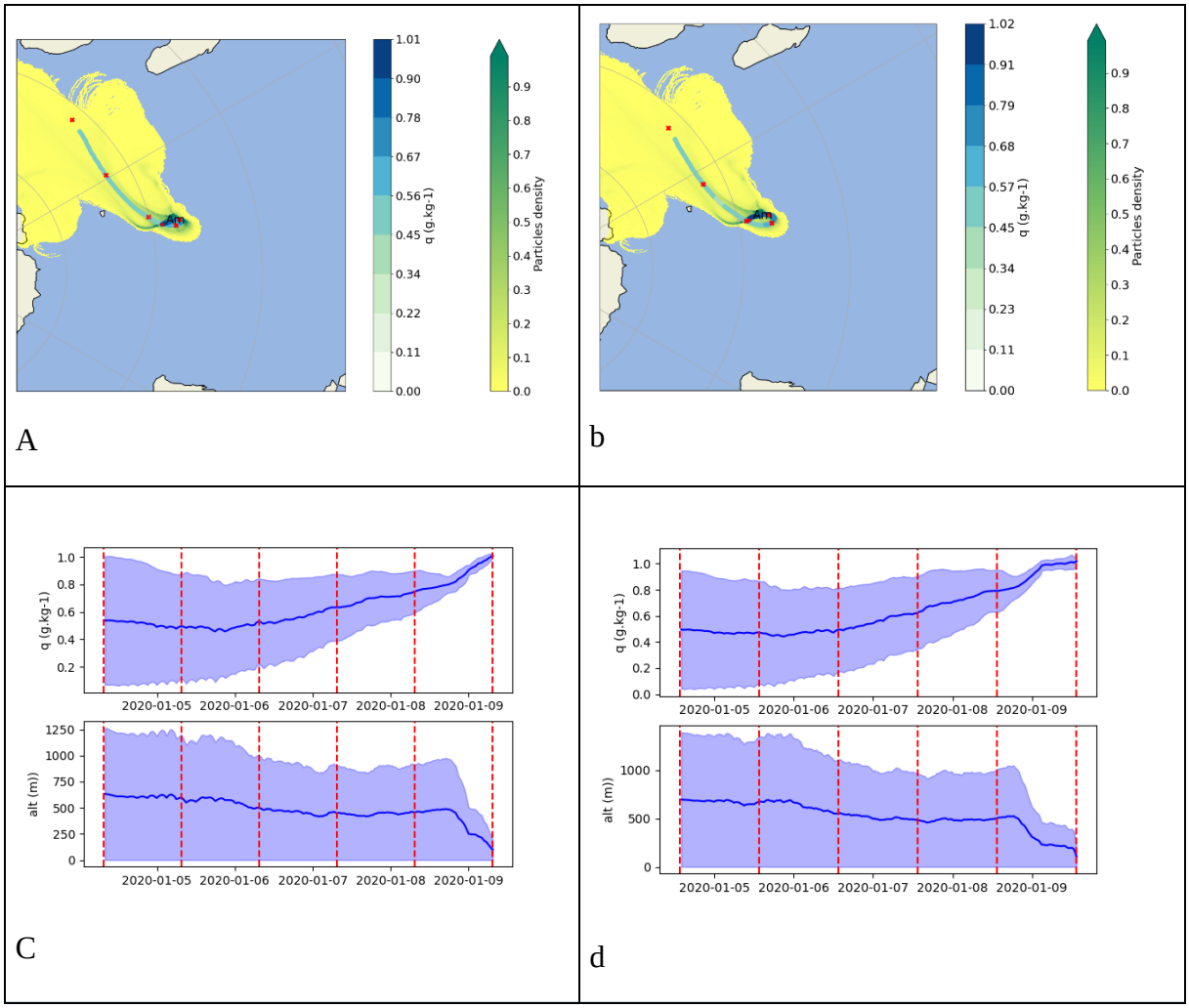

Figure A3: FLEXPART footprints of 5-day back trajectories for the event of January 9th 2020. Panel (a) Latitude-longitude projection of the FLEXPART back trajectory footprint for January 9th 2020 at 7h30. The yellow to green colors on each grid point of these projections represent the density of particles. The white to blue colors indicate the water vapor mixing ratio on the humidity weighted average back-trajectory. Each red point indicates the location of the average back-trajectory for each of the 5 days before the date of the considered event. Panel (b) Same as a for January 9th 2020 at 13h30. Panel (c) Top shows the evolution of the water vapor mixing ratio of the back trajectories for January 9th 2020 at 7h30; bottom shows the altitude evolution of the back trajectory for January 9th 2020 at 7h30. Panel (d) same as panel (c) for January 9th 2020 at 13h30.

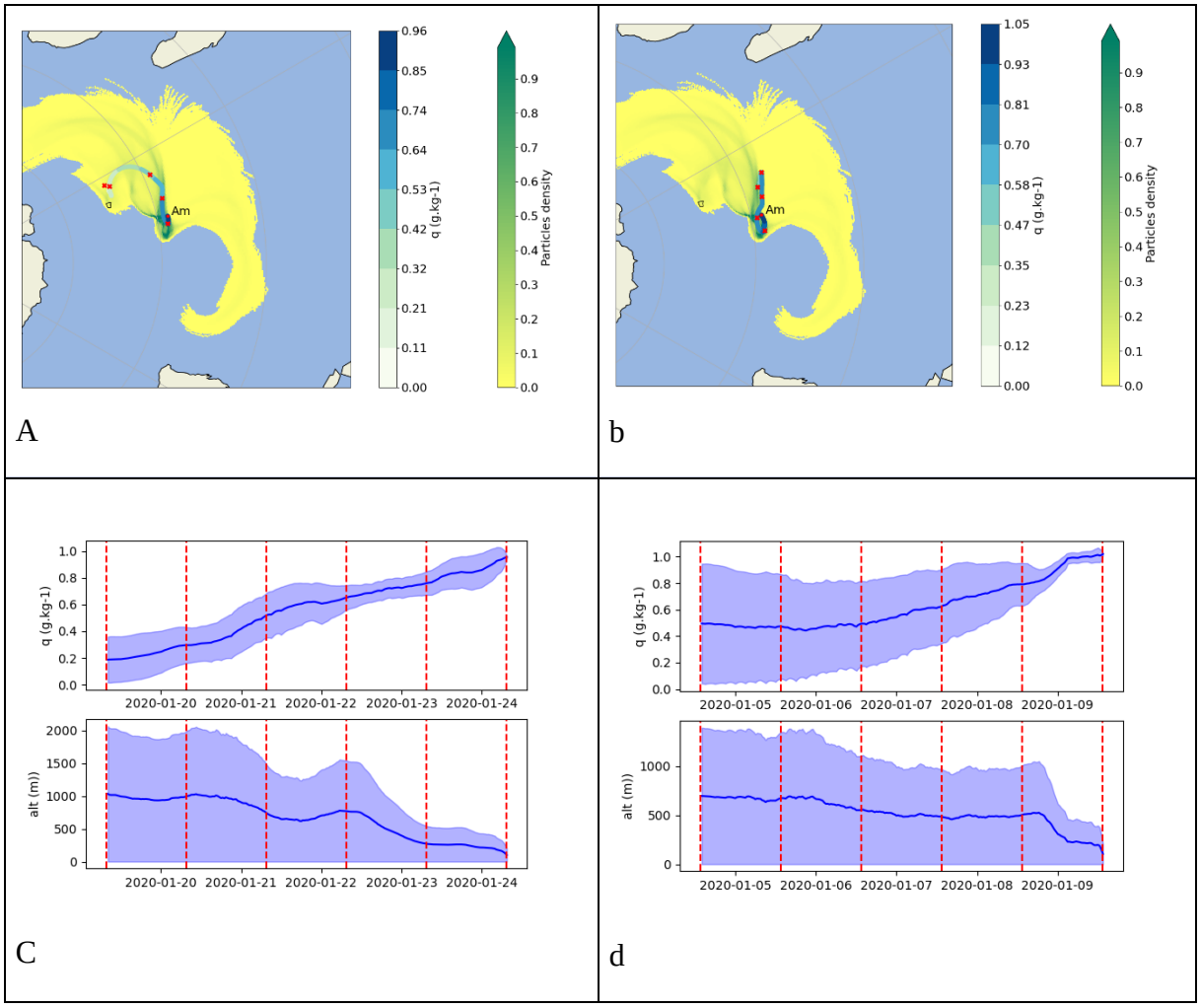

Figure A4: FLEXPART footprints of 5-day back trajectories for the event of January 21st 2020. (a) Latitude-longitude projection of the FLEXPART back trajectory footprint for January 21st 2020 at 7h30. The yellow to green colors on each grid point of these projections represent the density of particles. The white to blue colors indicate the water vapor mixing ratio on the humidity weighted average back-trajectory. Each red point indicates the location of the average back-trajectory for each of the 5 days before the date of the considered event. (b) Same as a for January 21st 2020 at 13h00. (c) Top shows the evolution of the water vapor mixing ratio of the back trajectories for January 21st 2020 at 7h30; bottom shows the altitude evolution of the back trajectory for January 21st 2020 at 7h30. (d) same as (c) for January 21st 2020 at 13h00.

Data availability: AMS L2 GEM data (https://doi.org/10.25326/168) are freely available (Magand and Dommergue, 2022) at https://gmos.aeris-data.fr/ from national GMOS-FR website data portal coordinated by IGE (Institut des Géosciences de l'Environnement, Grenoble, France; technical PI: Olivier Magand) with the support of the French national AERIS-SEDOO partners, data and services center for the atmosphere (last access: 08 December 2022). Hg species measurements belong to international monitoring networks (http://www.gos4m.org/). Water isotopic data and modeling outputs are available on the Zenodo platform (https://zenodo.org/record/8164392; https://zenodo.org/record/8160871).

Acknowledgements: We deeply thank all overwintering staff at AMS and the French Polar Institute Paul-Emile Victor (IPEV) staff and scientists who helped with the setup and maintenance of the experiment at AMS in the framework of the GMOStral-1028 IPEV program, the ICOS-416 program and the ADELISE-1205 IPEV program. Amsterdam Island Hg0 data, accessible in national GMOS-FR website data portal were collected via instruments coordinated by the IGE-PTICHA technical platform dedicated to atmospheric chemistry field instrumentation. GMOS-FR data portal is maintained by the French national center for Atmospheric data and services AERIS, which is acknowledged by the authors. The LMDZ-iso simulation were performed thanks to granted access to the HPC resources of IDRIS under the allocations 2022-AD010114000 and 2022-AD010107632R1 and made by GENCI. We deeply thank Sébastien Nguyen (CEA, LSCE) for his help and support in running LMDZiso simulation.

Funding: This work benefited from the IPSL-CGS EUR and was supported by a grant from the French government under the Programme d'Investissements d'avenir, reference ANR-11-IDEX-0004-17-EURE-0006, managed by the Agence Nationale de la Recherche. This project has also been supported by the LEFE IMAGO project ADELISE. Amsterdam Island GEM data, accessible in national GMOS-FR website data portal have been collected with funding from European Union 7th Framework Programme project Global Mercury Observation System (GMOS 2010-2015 Nr. 26511), the French Polar Institute IPEV via GMOStral-1028 IPEV program since 2012, the LEFE CHAT CNRS/INSU (TOPMMODEL project, Nr. AO2017-984931) and the H2020 ERA-PLANET (Nr. 689443) iGOSP program. This work is part of the AWACA project that has received funding from the European Research Council (ERC) under the European Union's Horizon 2020 research and innovation programme (Grant agreement No. 951596). The ERA5 reanalyses files for the ECHAM6-wiso nudging have been provided by

the German Climate Computing Center (DKRZ). The ECHAM6-wiso simulations have been performed with support of the Alfred Wegener Institute (AWI) supercomputing centre.

Author contributions: AL designed the study and analyzed the data together with FV, CS, EF, OM. OC installed the water vapor isotopic analyzer in Amsterdam Island and OJ was in charge of the data calibration. BM and FP performed the measurements of the isotopic composition of the precipitation samples. CA analyzed the modeling outputs, realized most of the simulations and performed model-data analyses. CLDS performed the back trajectory analyses with help from MC. OM, AD and YB provided expertise on GEM analyses and interpretation. AC, CR, ND and MW provided model simulations. AL wrote the paper with contribution of all coauthors.

Competing interests: One of the coauthors (AD) is a member of the editorial board of Atmospheric Chemistry and Physics.

References

Aemisegger, F., Sturm, P., Graf, P., Sodemann, H., Pfahl, S., Knohl, A., and Wernli, H.: Measuring variations of d18O and d2H in atmospheric water vapour using two commercial laser-based spectrometers: an instrument characterisation study, Atmospheric Measurement Techniques, 5, 1491–1511, https://doi.org/10.5194/amt-5-1491-2012, 2012.

Aemisegger, F., Spiegel, J., Pfahl, S., Sodemann, H., Eugster, W., and Wernli, H.: Isotope meteorology of cold front passages: A case study combining observations and modeling, Geophysical Research Letters, 42, 5652–5660, 2015.

Angot, H., Barret, M., Magand, O., Ramonet, M., and Dommergue, A.: A 2-year record of atmospheric mercury species at a background Southern Hemisphere station on Amsterdam Island, Atmospheric Chemistry and Physics, 14, 11461–11473, 2014.

Angot, H., Dion, I., Vogel, N., Legrand, M., Magand, O., and Dommergue, A.: Multi-year record of atmospheric mercury at Dumont d'Urville, East Antarctic coast: continental outflow and oceanic influences, Atmospheric Chemistry and Physics, 16, 8265–8279, 2016.

Ansari, M. A., Noble, J., Deodhar, A., and Kumar, U. S.: Atmospheric factors controlling the stable isotopes (δ18O and δ2H) of the Indian summer monsoon precipitation in a drying region of Eastern India, Journal of Hydrology, 584, 124636, 2020.

Arias, P., Bellouin, N., Coppola, E., Jones, R., Krinner, G., Marotzke, J., Naik, V., Palmer, M., Plattner, G.-K., Rogelj, J., and others: Climate Change 2021: the physical science basis. Contribution of Working Group I to the Sixth Assessment Report of the Intergovernmental Panel on Climate Change; technical summary, 2021.

Bailey, A., Aemisegger, F., Villiger, L., Los, S. A., Reverdin, G., Quiñones Meléndez, E., Acquistapace, C., Baranowski, D. B., Böck, T., Bony, S., Bordsdorff, T., Coffman, D., de Szoeke, S. P., Diekmann, C. J., Dütsch, M., Ertl, B., Galewsky, J., Henze, D., Makuch, P., Noone, D., Quinn, P. K., Rösch, M., Schneider, A., Schneider, M., Speich, S., Stevens, B., and Thompson, E. J.: Isotopic measurements in water vapor, precipitation, and seawater during EUREC^{4}A, Earth System Science Data, 15, 465–495, https://doi.org/10.5194/essd-15-465-2023, 2023.

Benetti, M., Reverdin, G., Pierre, C., Merlivat, L., Risi, C., Steen-larsen, H. C., and Vimeux, F.: Journal of Geophysical Research : Atmospheres during evaporation, 584–593, https://doi.org/10.1002/2013JD020535.Received, 2014.

Benetti, M., Aloisi, G., Reverdin, G., Risi, C., and Sèze, G.: Importance of boundary layer mixing for the isotopic composition of surface vapor over the subtropical North Atlantic Ocean, Journal of Geophysical Research: Atmospheres, 120, 2190–2209, 2015.

Bhattacharya, S. K., Sarkar, A., and Liang, M.-C.: Vapor isotope probing of typhoons invading the Taiwan region in 2016, Journal of Geophysical Research: Atmospheres, 127, e2022JD036578, 2022.

Bloom, N. and Fitzgerald, W. F.: Determination of volatile mercury species at the picogram level by low-temperature gas chromatography with cold-vapour atomic fluorescence detection, Analytica Chimica Acta, 208, 151–161, 1988.

Bonne, J. L., Behrens, M., Meyer, H., Kipfstuhl, S., Rabe, B., Schönicke, L., Steen-Larsen, H. C., and Werner, M.: Resolving the controls of water vapour isotopes in the Atlantic sector, Nature Communications, 10, 1–10, https://doi.org/10.1038/s41467-019-09242-6, 2019.

Boucher, O., Servonnat, J., Albright, A. L., Aumont, O., Balkanski, Y., Bastrikov, V., Bekki, S., Bonnet, R., Bony, S., Bopp, L., Braconnot, P., Brockmann, P., Cadule, P., Caubel, A., Cheruy, F.,

Codron, F., Cozic, A., Cugnet, D., D'Andrea, F., Davini, P., de Lavergne, C., Denvil, S., Deshayes, J., Devilliers, M., Ducharne, A., Dufresne, J.-L., Dupont, E., Éthé, C., Fairhead, L., Falletti, L., Flavoni, S., Foujols, M.-A., Gardoll, S., Gastineau, G., Ghattas, J., Grandpeix, J.-Y., Guenet, B., Guez, E., Lionel, Guilyardi, E., Guimberteau, M., Hauglustaine, D., Hourdin, F., Idelkadi, A., Joussaume, S., Kageyama, M., Khodri, M., Krinner, G., Lebas, N., Levavasseur, G., Lévy, C., Li, L., Lott, F., Lurton, T., Luyssaert, S., Madec, G., Madeleine, J.-B., Maignan, F., Marchand, M., Marti, O., Mellul, L., Meurdesoif, Y., Mignot, J., Musat, I., Ottlé, C., Peylin, P., Planton, Y., Polcher, J., Rio, C., Rochetin, N., Rousset, C., Sepulchre, P., Sima, A., Swingedouw, D., Thiéblemont, R., Traore, A. K., Vancoppenolle, M., Vial, J., Vialard, J., Viovy, N., and Vuichard, N.: Presentation and Evaluation of the IPSL-CM6A-LR Climate Model, Journal of Advances in Modeling Earth Systems, 12, e2019MS002010, https://doi.org/10.1029/2019MS002010, 2020.

Bréant, C., Leroy Dos Santos, C., Agosta, C., Casado, M., Fourré, E., Goursaud, S., Masson-Delmotte, V., Favier, V., Cattani, O., Prié, F., Golly, B., Orsi, A., Martinerie, P., and Landais, A.: Coastal water vapor isotopic composition driven by katabatic wind variability in summer at Dumont d'Urville, coastal East Antarctica, Earth and Planetary Science Letters, 514, 37–47, https://doi.org/10.1016/j.epsl.2019.03.004, 2019.

Brooks, S.; Ren, X. R.; Cohen, M.; Luke, W. T.; Kelley, P.; Artz, R.; Hynes, A.; Landing, W.; Martos, B. Airborne vertical profiling of mercury speciation near Tullahoma, TN, USA Atmosphere 2014, 5 (3) 557– 574 DOI: 10.3390/atmos5030557.

Casado, M., Landais, A., Masson-Delmotte, V., Genthon, C., Kerstel, E., Kassi, S., Arnaud, L., Picard, G., Prie, F., Cattani, O., Steen-Larsen, H.-C., Vignon, E., and Cermak, P.: Continuous measurements of isotopic composition of water vapour on the East Antarctic Plateau, Atmospheric Chemistry and Physics, 16, https://doi.org/10.5194/acp-16-8521-2016, 2016.

Cauquoin, A. and Werner, M.: High-Resolution Nudged Isotope Modeling With ECHAM6-Wiso: Impacts of Updated Model Physics and ERA5 Reanalysis Data, Journal of Advances in Modeling Earth Systems, 13, e2021MS002532, https://doi.org/10.1029/2021MS002532, 2021.

Cauquoin, A., Werner, M., and Lohmann, G.: Water isotopes -- climate relationships for the mid-Holocene and preindustrial period simulated with an isotope-enabled version of MPI-ESM, Climate of the Past, 15, 1913–1937, https://doi.org/10.5194/cp-15-1913-2019, 2019.

Craig, H.: Isotopic Variations in Meteoric Waters, Science, 133, 1702–1703, https://doi.org/10.1126/science.133.3465.1702, 1961.

Dahinden, F., Aemisegger, F., Wernli, H., Schneider, M., Diekmann, C. J., Ertl, B., Knippertz, P., Werner, M., and Pfahl, S.: Disentangling different moisture transport pathways over the eastern subtropical North Atlantic using multi-platform isotope observations and high-resolution numerical modelling, Atmospheric Chemistry and Physics, 21, 16319–16347, https://doi.org/10.5194/acp-21-16319-2021, 2021.

Dansgaard, W.: Stable isotopes in precipitation., Tellus, 16, 436–468, 1964.

Dumarey, R., Temmerman, E., Adams, R., and Hoste, J.: The accuracy of the vapour-injection calibration method for the determination of mercury by amalgamation/cold-vapour atomic absorption spectrometry, Analytica Chimica Acta, 170, 337–340, 1985.

Durack, P. J., Taylor, K. E., Ames, S., Po-Chedley, S., and Mauzey, C.: PCMDI AMIP SST and sea-ice boundary conditions version 1.1.8, , https://doi.org/10.22033/ESGF/input4MIPs.16921, 2022.

Dütsch, M., Pfahl, S., and Wernli, H.: Drivers of δ2H variations in an idealized extratropical cyclone, Geophysical Research Letters, 43, 5401–5408, 2016.

Edwards, B. A., Kushner, D. S., Outridge, P. M., Wang, F. (2021). Fifty years of volcanic mercury emission research: Knowledge gaps and future directions. *Science of The Total Environment*, *757*, 143800. https://doi.org/10.1016/j.scitotenv.2020.143800.

El Yazidi, A., Ramonet, M., Ciais, P., Broquet, G., Pison, I., Abbaris, A., Brunner, D., Conil, S., Delmotte, M., Gheusi, F., and others: Identification of spikes associated with local sources in continuous time series of atmospheric CO, CO_2 and CH_4, Atmospheric Measurement Techniques, 11, 1599–1614, 2018.

Eyring, V., Bony, S., Meehl, G. A., Senior, C. A., Stevens, B., Stouffer, R. J., and Taylor, K. E.: Overview of the Coupled Model Intercomparison Project Phase 6 (CMIP6) experimental design and organization, Geoscientific Model Development, 9, 1937–1958, https://doi.org/10.5194/gmd-9-1937-2016, 2016.

Fain, X.; Obrist, D.; Hallar, A. G.; Mccubbin, I.; Rahn, T. High levels of reactive gaseous mercury observed at a high elevation research laboratory in the Rocky Mountains Atmos. Chem. Phys. 2009, 9 (20) 8049– 8060 DOI: 10.5194/acp-9-8049-2009.

Fitzgerald, W. F. and Gill, G. A.: Subnanogram determination of mercury by two-stage gold amalgamation and gas phase detection applied to atmospheric analysis, Analytical chemistry, 51, 1714–1720, 1979.

Fogt, R. and Marshall, G.: The Southern Annular Mode: Variability, trends, and climate impacts across the Southern Hemisphere, Wiley Interdisciplinary Reviews: Climate Change, 11, https://doi.org/10.1002/wcc.652, 2020.

Fu, X., Marusczak, N., Wang, X., Gheusi, F. and Sonke, J.: The isotopic composition of gaseous elemental mercury in the free troposphere of the Pic du Midi Observatory, France. Environmental Science & Technology. 50. 10.1021/acs.est.6b00033, 2016

Galewsky, J., Steen-Larsen, H. C., Field, R. D., Worden, J., Risi, C., and Schneider, M.: Stable isotopes in atmospheric water vapor and applications to the hydrologic cycle, Reviews of Geophysics, 54, 809–865, 2016.

Gaudry, A., Ascencio, J., and Lambert, G.: Preliminary study of CO2 variations at Amsterdam Island (Territoire des Terres Australes et Antarctiques Francaises), Journal of Geophysical Research: Oceans, 88, 1323–1329, 1983.

Graf, P., Wernli, H., Pfahl, S., and Sodemann, H.: A new interpretative framework for below-cloud effects on stable water isotopes in vapour and rain, Atmospheric Chemistry and Physics, 19, 747–765, 2019.

Gros, V., Poisson, N., Martin, D., Kanakidou, M., and Bonsang, B.: Observations and modeling of the seasonal variation of surface ozone at Amsterdam Island: 1994–1996, Journal of Geophysical Research: Atmospheres, 103, 28103–28109, 1998.

Gros, V., Bonsang, B., Martin, D., Novelli, P., and Kazan, V.: Carbon monoxide short term measurements at Amsterdam island: estimations of biomass burning emission rates, Chemosphere-Global Change Science, 1, 163–172, 1999.

Gaffney J, Marley N. In-depth review of atmospheric mercury: sources, transformations, and potential sinks. *Energy and Emission Control Technologies*. 2014;2:1-21https://doi.org/10.2147/EECT.S37038.

Guilpart, E., Vimeux, F., Evan, S., Brioude, J., Metzger, J., Barthe, C., Risi, C., and Cattani, O.: The isotopic composition of near-surface water vapor at the Maïdo observatory (Reunion Island,

southwestern Indian Ocean) documents the controls of the humidity of the subtropical troposphere, Journal of Geophysical Research: Atmospheres, 122, 9628–9650, https://doi.org/10.1002/2017JD026791, 2017.

Gustin, M. S., Amos, H. M., Huang, J., Miller, M. B., and Heidecorn, K.: Measuring and modeling mercury in the atmosphere: a critical review, Atmos. Chem. Phys., 15, 5697–5713, https://doi.org/10.5194/acp-15-5697-2015, 2015.

Gustin, M. S., Bank, M. S., Bishop, K., Bowman, K., Brafireun, B., Chételat, J., Eckley, C. S., Hammerschmidt, C. R., Lamborg, C., Lyman, S., Martínez-Cortizas, A., Sommar, J., Tsz-Ki Tsui, M., & Zhang, T. (2020). Mercury biogeochemical cycling: A synthesis of recent scientific advances. Science of the Total Environment, 737, 139619. https://doi.org/10.1016/j.scitotenv.2020.139619.

Gworek, B., Dmuchowski, W. & Baczewska-Dąbrowska, A.H. Mercury in the terrestrial environment: a review. Environ Sci Eur **32**, 128 (2020). https://doi.org/10.1186/s12302-020-00401-x.

Henze, D., Noone, D., and Toohey, D.: Aircraft measurements of water vapor heavy isotope ratios in the marine boundary layer and lower troposphere during ORACLES, Earth Syst. Sci. Data, 14, 1811–1829, https://doi.org/10.5194/essd-14-1811-2022, 2022.

Hersbach, H., Bell, B., Berrisford, P., Hirahara, S., Horányi, A., Muñoz-Sabater, J., Nicolas, J., Peubey, C., Radu, R., Schepers, D., Simmons, A., Soci, C., Abdalla, S., Abellan, X., Balsamo, G., Bechtold, P., Biavati, G., Bidlot, J., Bonavita, M., De Chiara, G., Dahlgren, P., Dee, D., Diamantakis, M., Dragani, R., Flemming, J., Forbes, R., Fuentes, M., Geer, A., Haimberger, L., Healy, S., Hogan, R. J., Hólm, E., Janisková, M., Keeley, S., Laloyaux, P., Lopez, P., Lupu, C., Radnoti, G., de Rosnay, P., Rozum, I., Vamborg, F., Villaume, S., and Thépaut, J.-N.: The ERA5 global reanalysis, Quarterly Journal of the Royal Meteorological Society, 146, 1999–2049, https://doi.org/10.1002/qj.3803, 2020.

Hoang, C., Magand, O., Brioude, J., Dimuro, A., Brunet, C., Ah-Peng, C., Bertrand, Y., Dommergue, A., Lei, Y. D., and Wania, F.: Probing the limits of sampling gaseous elemental mercury passively in the remote atmosphere, Environ. Sci.: Atmos., 3, 268–281, https://doi.org/10.1039/D2EA00119E, 2023.

Hourdin, F., Rio, C., Grandpeix, J.-Y., Madeleine, J.-B., Cheruy, F., Rochetin, N., Jam, A., Musat, I., Idelkadi, A., Fairhead, L., Foujols, M.-A., Mellul, L., Traore, A.-K., Dufresne, J.-L., Boucher, O., Lefebvre, M.-P., Millour, E., Vignon, E., Jouhaud, J., Diallo, F. B., Lott, F., Gastineau, G., Caubel, A., Meurdesoif, Y., and Ghattas, J.: LMDZ6A: The Atmospheric Component of the IPSL Climate Model With Improved and Better Tuned Physics, Journal of Advances in Modeling Earth Systems, 12, e2019MS001892, https://doi.org/10.1029/2019MS001892, 2020.

Jiskra, M., Sonke, J. E., Obrist, D., Bieser, J., Ebinghaus, R., Myhre, C. L., Pfaffhuber, K. A., Wängberg, I., Kyllönen, K., Worthy, D., Martin, L. G., Labuschagne, C., Mkololo, T., Ramonet, M., Magand, O., and Dommergue, A.: A vegetation control on seasonal variations in global atmospheric mercury concentrations, Nature Geoscience, 11, 244–250, https://doi.org/10.1038/s41561-018-0078-8, 2018.

Jullien, N., Vignon, É., Sprenger, M., Aemisegger, F., and Berne, A.: Synoptic conditions and atmospheric moisture pathways associated with virga and precipitation over coastal Adélie Land in Antarctica, The Cryosphere, 14, 1685–1702, https://doi.org/10.5194/tc-14-1685-2020, 2020.

Koening, A.M., Magand, O., Verreyken, B., Brioude, J., Amelynck, C., Schoon, N., Colomb, A., Ramonet, M., Sha, M.K., Cammas, J.P., Sonke, J.E., Dommergue, A., 2023. Mercury in the free troposphere and bidirectional atmosphere-vegetation exchanges – Insights from Maido observatory in the southern hemisphere tropics. Atmos. Chem. Phys., 23, 1309-1328, https://doi.org/10.5194/acp-23-1309-2023

Lee, K.-O., Aemisegger, F., Pfahl, S., Flamant, C., Lacour, J.-L., and Chaboureau, J.-P.: Contrasting stable water isotope signals from convective and large-scale precipitation phases of a heavy precipitation event in southern Italy during HyMeX IOP 13: a modelling perspective, Atmospheric Chemistry and Physics, 19, 7487–7506, 2019.

LeGrande, A. N. and Schmidt, G. A.: Global gridded data set of the oxygen isotopic composition in seawater, Geophysical Research Letters, 33, 1–5, https://doi.org/10.1029/2006GL026011, 2006.

Leroy-Dos Santos, C., Masson-Delmotte, V., Casado, M., Fourré, E., Steen-Larsen, H. C., Maturilli, M., Orsi, A., Berchet, A., Cattani, O., Minster, B., Gherardi, J., and Landais, A.: A 4.5 Year-Long Record of Svalbard Water Vapor Isotopic Composition Documents Winter Air Mass Origin, Journal of Geophysical Research: Atmospheres, 125, e2020JD032681-e2020JD032681, https://doi.org/10.1029/2020JD032681, 2020.

Leroy-Dos Santos, C., Casado, M., Prié, F., Jossoud, O., Kerstel, E., Farradèche, M., Kassi, S., Fourré, E., and Landais, A.: A dedicated robust instrument for water vapor generation at low humidity for use with a laser water isotope analyzer in cold and dry polar regions, Atmospheric Measurement Techniques, 14, 2907–2918, https://doi.org/10.5194/amt-14-2907-2021, 2021.

Li, C., Enrico, M., Magand, O., Araujo, B. F., Le Roux, G., Osterwalder, S., Dommergue, A., Bertrand, Y., Brioude, J., De Vleeschouwer, F., and others: A peat core Hg stable isotope reconstruction of Holocene atmospheric Hg deposition at Amsterdam Island (37.8 oS), Geochimica et Cosmochimica Acta, 341, 62–74, 2023.

Lindberg, S., Bullock, R., Ebinghaus, R., Engstrom, D., Feng, X., Fitzgerald, W., Pirrone, N., Prestbo, E., and Seigneur, C.: A synthesis of progress and uncertainties in attributing the sources of mercury in deposition., Ambio, 36, 19–32, 2007, https://doi.org/10.1579/0044-7447(2007)

Lyman, S. N.; Jaffe, D. A. Formation and fate of oxidized mercury in the upper troposphere and lower stratosphere Nat. Geosci. 2012, 5 (2) 114– 117 doi: 10.1038/ngeo1353

Magand, O. and Dommergue, A.: Continuous measurements of atmospheric mercury at Maido Observatory (L2), Global Mercury Observation System [data set], 2022.

Munksgaard, N. C., Zwart, C., Kurita, N., Bass, A., Nott, J., and Bird, M. I.: Stable isotope anatomy of tropical cyclone Ita, north-eastern Australia, April 2014, PloS one, 10, e0119728, 2015.

Murphy, D. M.; Hudson, P. K.; Thomson, D. S.; Sheridan, P. J.; Wilson, J. C. Observations of Mercury-Containing Aerosols. Environ. Sci. Technol. 2006, 40 (10), 3163–3167.

Noone, D.: Pairing Measurements of the Water Vapor Isotope Ratio with Humidity to Deduce Atmospheric Moistening and Dehydration in the Tropical Midtroposphere, Journal of Climate, 25, 4476–4494, https://doi.org/10.1175/JCLI-D-11-00582.1, 2012.

Pisso, I., Sollum, E., Grythe, H., Kristiansen, N. I., Cassiani, M., Eckhardt, S., Arnold, D., Morton, D., Thompson, R. L., Groot Zwaaftink, C. D., Evangeliou, N., Sodemann, H., Haimberger, L., Henne, S., Brunner, D., Burkhart, J. F., Fouilloux, A., Brioude, J., Philipp, A., Seibert, P., and Stohl, A.: The Lagrangian particle dispersion model FLEXPART version 10.4, Geoscientific Model Development, 12, 4955–4997, https://doi.org/10.5194/gmd-12-4955-2019, 2019.

Polian, G., Lambert, G., Ardouin, B., and Jegou, A.: Long-range transport of continental radon in subantarctic and antarctic areas, Tellus B: Chemical and Physical Meteorology, 38, 178–189, 1986.

Risi, C., Bony, S., Vimeux, F., and Jouzel, J.: Water-stable isotopes in the LMDZ4 general circulation model: Model evaluation for present-day and past climates and applications to climatic interpretations

of tropical isotopic records, Journal of Geophysical Research Atmospheres, 115, https://doi.org/10.1029/2009JD013255, 2010.

Ryan, B.F., J.J. Katzfey, D.J. Abbs, C. Jakob, U. Lohmann, B. Rockel, L.D. Rotstayn, R.E. Stewart, K.K. Szeto, G. Tselioudis, and M.K. Yau, 2000: Simulations of a cold front by cloud-resolving, limited-area, and large-scale models, and a model evaluation using in situ and satellite observations. *Mon. Weather Rev.*, **128**, 3218-3235, doi:10.1175/1520-0493(2000)

Sciare, J., Mihalopoulos, N., and Dentener, F.: Interannual variability of atmospheric dimethylsulfide in the southern Indian Ocean, Journal of Geophysical Research: Atmospheres, 105, 26369–26377, 2000.

Sciare, J., Favez, O., Sarda-Estève, R., Oikonomou, K., Cachier, H., and Kazan, V.: Long-term observations of carbonaceous aerosols in the Austral Ocean atmosphere: Evidence of a biogenic marine organic source, Journal of Geophysical Research: Atmospheres, 114, 2009.

Shah, V., Jacob, D. J., Thackray, C. P., Wang, X., Sunderland, E. M., Dibble, T. S., Saiz-Lopez, A., Cˇ ernušák, I., Kellö, V., astro, P. J., Wu, R., and Wang, C.: Improved Mechanistic Model of the Atmospheric Redox Chemistry of Mercury, Environ. Sci. Technol., 55, 14445–14456, https://doi.org/10.1021/acs.est.1c03160, 2021.

Sheu, G. R.; Lin, N. H.; Wang, J. L.; Lee, C. T.; Yang, C. F. O.; Wang, S. H. Temporal distribution and potential sources of atmospheric mercury measured at a high-elevation background station in Taiwan Atmos. Environ. 2010, 44 (20) 2393– 2400 DOI: 10.1016/j.atmosenv.2010.04.009

Sherwood, S. C., Bony, S., and Dufresne, J.-L.: Spread in model climate sensitivity traced to atmospheric convective mixing, Nature, 505, 37–42, https://doi.org/10.1038/nature12829, 2014.

Sillman, S., Marsik, F. J., Al-Wali, K. I., Keeler, G. J., and Landis, M. S.: Reactive mercury in the troposphere: Model formation and results for Florida, the northeastern United States, and the Atlantic Ocean, Journal of Geophysical Research: Atmospheres, 112, 2007.

Slemr, F., Angot, H., Dommergue, A., Magand, O., Barret, M., Weigelt, A., Ebinghaus, R., Brunke, E.-G., Pfaffhuber, K. A., Edwards, G., and others: Comparison of mercury concentrations measured at several sites in the Southern Hemisphere, Atmospheric Chemistry and Physics, 15, 3125–3133, 2015.

Slemr, F., Martin, L., Labuschagne, C., Mkololo, T., Angot, H., Magand, O., Dommergue, A., Garat, P., Ramonet, M., and Bieser, J.: Atmospheric mercury in the Southern Hemisphere–Part 1: Trend and inter-annual variations in atmospheric mercury at Cape Point, South Africa, in 2007–2017, and on Amsterdam Island in 2012–2017, Atmospheric Chemistry and Physics, 20, 7683–7692, 2020.

Sprovieri, F., Pirrone, N., Bencardino, M., D'amore, F., Carbone, F., Cinnirella, S., Mannarino, V., Landis, M., Ebinghaus, R., Weigelt, A., and others: Atmospheric mercury concentrations observed at ground-based monitoring sites globally distributed in the framework of the GMOS network, Atmospheric chemistry and physics, 16, 11915–11935, 2016.

Steen-Larsen, H. C., Johnsen, S. J., Masson-Delmotte, V., Stenni, B., Risi, C., Sodemann, H., Balslev-Clausen, D., Blunier, T., Dahl-Jensen, D., Elleh??j, M. D., Falourd, S., Grindsted, A., Gkinis, V., Jouzel, J., Popp, T., Sheldon, S., Simonsen, S. B., Sjolte, J., Steffensen, J. P., Sperlich, P., Sveinbj??rnsd??ttir, A. E., Vinther, B. M., and White, J. W. C.: Continuous monitoring of summer surface water vapor isotopic composition above the Greenland Ice Sheet, Atmospheric Chemistry and Physics, 13, 4815–4828, https://doi.org/10.5194/acp-13-4815-2013, 2013.

Steffen, A., Scherz, T., Olson, M., Gay, D., and Blanchard, P.: A comparison of data quality control protocols for atmospheric mercury speciation measurements, Journal of Environmental Monitoring, 14, 752–765, 2012.

Stevens, B., Giorgetta, M., Esch, M., Mauritsen, T., Crueger, T., Rast, S., Salzmann, M., Schmidt, H., Bader, J., Block, K., Brokopf, R., Fast, I., Kinne, S., Kornblueh, L., Lohmann, U., Pincus, R., Reichler, T., and Roeckner, E.: Atmospheric component of the MPI-M Earth System Model: ECHAM6, Journal of Advances in Modeling Earth Systems, 5, 146–172, https://doi.org/10.1002/jame.20015, 2013.

Swartzendruber, P., Chand, D., Jaffe, D., Smith, J., Reidmiller, D., Gratz, L., Keeler, J., Strode, S., Jaeglé, L., and Talbot, R.: Vertical distribution of mercury, CO, ozone, and aerosol scattering coefficient in the Pacific Northwest during the spring 2006 INTEX-B campaign, Journal of Geophysical Research: Atmospheres, 113, 2008.

Swartzendruber, P. C., Jaffe, D. A., Prestbo, E., Weiss-Penzias, P., Selin, N. E., Park, R., Jacob, D. J., Strode, S., and Jaegle, L.: Observations of reactive gaseous mercury in the free troposphere at the Mount Bachelor Observatory, Journal of Geophysical Research: Atmospheres, 111, 2006.

Swartzendruber, P.; Chand, D.; Jaffe, D. A.; Smith, J.; Reidmiller, D.; Gratz, L.; Keeler, J.; Strode, S.; Jaegle, L.; Talbot, R. Vertical distribution of mercury, CO, ozone, and aerosol scattering coefficient in the Pacific Northwest during the spring 2006 INTEX-B campaign. J. Geophys. Res., [Atmos.] 2008, 113, D10305.

Talbot, R., Mao, H., Scheuer, E., Dibb, J., and Avery, M.: Total depletion of Hg in the upper troposphere–lower stratosphere, Geophysical Research Letters, 34, 2007.

Talbot, R., Mao, H., Scheuer, E., Dibb, J., Avery, M., Browell, E., Sachse, G., Vay, S., Blake, D., Huey, G., and others: Factors influencing the large-scale distribution of Hg° in the Mexico City area and over the North Pacific, Atmospheric Chemistry and Physics, 8, 2103–2114, 2008.

Taylor, K. E., Williamson, D., and Zwiers, F.: The sea surface temperature and sea ice concentration boundary conditions for AMIP II simulations", PCMDI Report 60, Program for Climate Model Diagnosis and Intercomparison,Lawrence Livermore National Laboratory, 2000.

Thurnherr, I., Kozachek, A., Graf, P., Weng, Y., Bolshiyanov, D., Landwehr, S., Pfahl, S., Schmale, J., Sodemann, H., Steen-Larsen, H. C., and others: Meridional and vertical variations of the water vapour isotopic composition in the marine boundary layer over the Atlantic and Southern Ocean, Atmospheric Chemistry and Physics, 20, 5811–5835, 2020.

Tremoy, G., Vimeux, F., Cattani, O., Mayaki, S., Souley, I., and Favreau, G.: Measurements of water vapor isotope ratios with wavelength-scanned cavity ring-down spectroscopy technology: New insights and important caveats for deuterium excess measurements in tropical areas in comparison with isotope-ratio mass spectrometry, Rapid Communications in Mass Spectrometry, 25, 3469–3480, https://doi.org/10.1002/rcm.5252, 2011.

Tremoy, G., Vimeux, F., Mayaki, S., Souley, I., Cattani, O., Risi, C., Favreau, G., and Oi, M.: A 1-year long δ18O record of water vapor in Niamey (Niger) reveals insightful atmospheric processes at different timescales, Geophysical Research Letters, 39, 2012.

Tremoy, G., Vimeux, F., Soumana, S., Souley, I., Risi, C., Favreau, G., and Oï, M.: Clustering mesoscale convective systems with laser-based water vapor δ18O monitoring in Niamey (Niger), Journal of Geophysical Research: Atmospheres, 119, 5079–5103, https://doi.org/10.1002/2013JD020968, 2014.

Wang, H., Fyke, J. G., Lenaerts, J. T. M., Nusbaumer, J. M., Singh, H., Noone, D., Rasch, P. J., and Zhang, R.: Influence of sea-ice anomalies on Antarctic precipitation using source attribution in the Community Earth System Model, The Cryosphere, 14, 429–444, https://doi.org/10.5194/tc-14-429-2020, 2020.

Weiss-Penzias, P.; Gustin, M. S.; Lyman, S. N. Observations of speciated atmospheric mercury at three sites in Nevada: Evidence for a free tropospheric source of reactive gaseous mercury. J. Geophys. Res. [Atmos.] 2009, 114, D14302.

Weng, Y., Touzeau, A., and Sodemann, H.: Correcting the impact of the isotope composition on the mixing ratio dependency of water vapour isotope measurements with cavity ring-down spectrometers, Atmospheric Measurement Techniques, 13, 3167–3190, https://doi.org/10.5194/amt-13-3167-2020, 2020.

Worden, J., Noone, D., and Bowman, K.: Importance of rain evaporation and continental convection in the tropical water cycle., Nature, 445, 528–532, https://doi.org/10.1038/nature05508, 2007.